



HAL
open science

DART: Improvement of thermal infrared radiative transfer modelling for simulating top of atmosphere radiance

Ying-Jie Wang, Jean-Philippe Gastellu-Etchegorry

► **To cite this version:**

Ying-Jie Wang, Jean-Philippe Gastellu-Etchegorry. DART: Improvement of thermal infrared radiative transfer modelling for simulating top of atmosphere radiance. *Remote Sensing of Environment*, 2020, 251, pp.112082. 10.1016/j.rse.2020.112082 . hal-03082738

HAL Id: hal-03082738

<https://hal.science/hal-03082738>

Submitted on 18 Dec 2020

HAL is a multi-disciplinary open access archive for the deposit and dissemination of scientific research documents, whether they are published or not. The documents may come from teaching and research institutions in France or abroad, or from public or private research centers.

L'archive ouverte pluridisciplinaire **HAL**, est destinée au dépôt et à la diffusion de documents scientifiques de niveau recherche, publiés ou non, émanant des établissements d'enseignement et de recherche français ou étrangers, des laboratoires publics ou privés.

1 DART: improvement of thermal infrared radiative transfer 2 modelling for simulating top of atmosphere radiance

3
4 Yingjie WANG¹, Jean-Philippe Gastellu-Etchegorry¹

5
6 ¹ CESBIO, CNES-CNRS-IRD-UPS, University of Toulouse, 31401 Toulouse CEDEX 09,
7 France

8
9 Correspondence to: Yingjie WANG (yingjiewang1102@gmail.com)

10 11 **Abstract**

12
13 Land surface temperature (LST) is increasingly needed for studying the functioning of the
14 Earth's surface at local to global scale. Radiative transfer (RT) models that simulate top of
15 atmosphere (TOA) radiance are essential tools to derive accurate LST from thermal infrared
16 (TIR) signals of Earth observation (EO) satellites. DART (Discrete Anisotropic Radiative
17 Transfer) is one of the most accurate and comprehensive three-dimensional models that
18 simulate RT in the Earth-atmosphere system. Up to version 5.7.3, the mean absolute error
19 (MAE) of DART atmospheric TIR radiance of six standard atmospheres (USSTD76,
20 TROPICAL, MIDLATSUM, MIDLATWIN, SUBARCSUM, SUBARCWIN) over 3.5 μm
21 - 20 μm was 3.1 K compared to the reference atmospheric RT model MODTRAN, which is
22 much larger than the 1 K accuracy needed by most LST applications. Also, the radiance error
23 reached 2.6 K for some TIR bands whereas the noise equivalent differential temperature (NeDT)

24 of satellite TIR sensor is usually less than 0.4 K. Recently, the DART atmospheric RT
25 modelling was greatly improved by (1) introducing the equivalent absorption cross-section of
26 five most absorbing gases (H₂O, CO₂, O₃, CH₄, N₂O), and (2) implementing a double-layer
27 thermal emission method. The MAE of DART atmospheric TIR radiance of six standard
28 atmospheres and actual atmospheres over France and the Mediterranean Sea is now better than
29 1.0 K. The band radiance error is less than 0.2 K in the EO satellite TIR bands. DART is still
30 accurate if the temperature profiles of standard atmospheres are offset by less than 6 K and if
31 the viewing zenith angle is less than 50°. In short, the improved DART meets the requirements
32 of both LST applications, and present and future TIR EO satellite missions. It is already
33 available to scientists (<https://dart.omp.eu>).

34

35 **Keywords:** DART, radiative transfer, atmosphere, thermal infrared, absorption cross-section,
36 MODTRAN

37

38 1. Introduction

39

40 Land surface temperature (LST) has a wide range of applications in different fields:
41 evapotranspiration, soil moisture, precision agriculture, urban climate, river environments,
42 oceanography, *etc.* (Dugdale, 2016; Khanal et al., 2017; Kilpatrick et al., 2015; Voogt and Oke,
43 2003; Wang et al., 2006; Wang and Qu, 2009). Due to its high temporal resolution, broad
44 coverage and low cost, thermal infrared (TIR) remote sensing is an ideal tool to measure LST
45 (Li et al., 2013). Therefore, an increasing number of space missions embark sensors with TIR
46 bands. For example, the Trishna mission of French Space Agency (CNES) and Indian Space
47 Research Organization (ISRO), to be launched in 2024-2025, will embark a sensor that has four
48 TIR bands with noise equivalent differential temperature (NeDT) of 0.3 K at 300 K (Lagouarde

49 et al., 2018). The sea and land surface temperature radiometer on board the European Space
50 Agency (ESA) Sentinel 3 satellite has three TIR bands with NeDT of 0.05 K at 270 K (Donlon
51 et al., 2012). The National Aeronautics and Space Administration (NASA) Landsat 8 satellite
52 has a TIR sensor with NeDT of 0.4 K at 300 K (Irons et al., 2012). Landsat 9 satellite, due to
53 be launched on 2021, should embark a TIR sensor similar to the Landsat 8 TIR sensor
54 (McCorkel et al., 2018).

55

56 Most LST applications require accuracy less than 1 K (Sobrino et al., 2016). Although the
57 sensibility (NeDT) of most satellite TIR sensors is less than 0.4 K, the LST derived from
58 remotely sensed data is usually less accurate, mainly due to atmospheric conditions, topography,
59 land surface heterogeneity, and directional effects (Bento et al., 2017; Bonafoni, 2016; Ermida
60 et al., 2018; He et al., 2019; Price, 1983; Vermote et al., 2002). Therefore, there is a need to
61 better link LST and observations from satellite TIR sensors. Physical models that accurately
62 simulate TIR radiative transfer (RT) in the Earth-atmosphere system are essential tools.
63 However, most RT models are either for the atmosphere (*e.g.*, 4A/OP, MODTRAN, LBLRTM,
64 RFM, ARTS) or for the Earth surfaces (*e.g.*, Rayspread, RAPID3, FLiES, SAIL) (Berk et al.,
65 2015; Buehler et al., 2018; Clough et al., 2005; Huang, 2018; Kobayashi and Iwabuchi, 2008;
66 Scott, 1974; Verhoef, 1984; Vincent and Dudhia, 2017; Widlowski et al., 2006). DART
67 (Discrete Anisotropic Radiative Transfer) is one of the few models that simulate RT in the
68 Earth-atmosphere system. Its Earth surface RT modelling accuracy in the short and long waves
69 was already verified in the four phases of the RAdiative transfer Model Intercomparison (RAMI)
70 project (Widlowski et al., 2015, 2013, 2007) and in experiments (Guillevic et al., 2003, 2013).
71 Its atmospheric short wave RT modelling was validated with the reference atmospheric RT
72 model MODTRAN-5 (Gastellu-Etchegorry et al., 2017; Grau and Gastellu-Etchegorry, 2013).

73 However, as presented below, its atmospheric RT modelling in the TIR region did not meet the
74 requirements of LST applications and TIR Earth observation (EO) satellite missions.

75

76 DART simulates atmosphere in three altitude regions: (1) the bottom atmosphere inside the
77 Earth scene voxel matrix, (2) the mid-atmosphere made of voxels of any size, and (3) the high
78 atmosphere made of layers. Voxels in the mid-atmosphere allows DART to simulate the spatial
79 heterogeneity of the atmosphere backscattering. Any atmosphere layer is homogeneously filled
80 with gasses, aerosols and/or clouds that have specific physical (*i.e.*, temperature, pressure,
81 density) and spectral (*i.e.*, absorption/scattering extinction coefficient, scattering phase function)
82 properties. The atmospheric RT modelling relies on the spectral application of Beer's law and
83 band mean optical properties (Gastellu-Etchegorry et al., 2004). The extinction coefficient at
84 each layer is calculated so that the use of Beer's law gives the same vertical atmospheric
85 transmittance as MODTRAN, assuming that the cross-section of the gases is independent of
86 pressure and temperature. Although initial methodology simulates accurate atmospheric
87 radiance in short waves, the TIR radiance could differ significantly from MODTRAN. For
88 example, in $[3.5 \mu\text{m} - 20 \mu\text{m}]$ region, its mean absolute error (MAE) of top of atmosphere (TOA)
89 atmospheric TIR brightness temperature (BT) of the USSTD76 atmosphere was 3.1 K, which
90 is much larger than LST application requirements. This is due to three approximations: (1) gas
91 absorption cross-section is independent of pressure and temperature; (2) gas absorption
92 transmittance is computed with Beer's law and band mean optical properties; (3) the method
93 that computes layer thermal emission is only suited to optically thin atmosphere.

94

95 Actually, the gas absorption cross-section varies with pressure and temperature due to the
96 Doppler and Lorentz broadening. Many atmospheric RT models, including MODTRAN,
97 compute the pressure- and temperature-dependent gas absorption cross-section lines based on

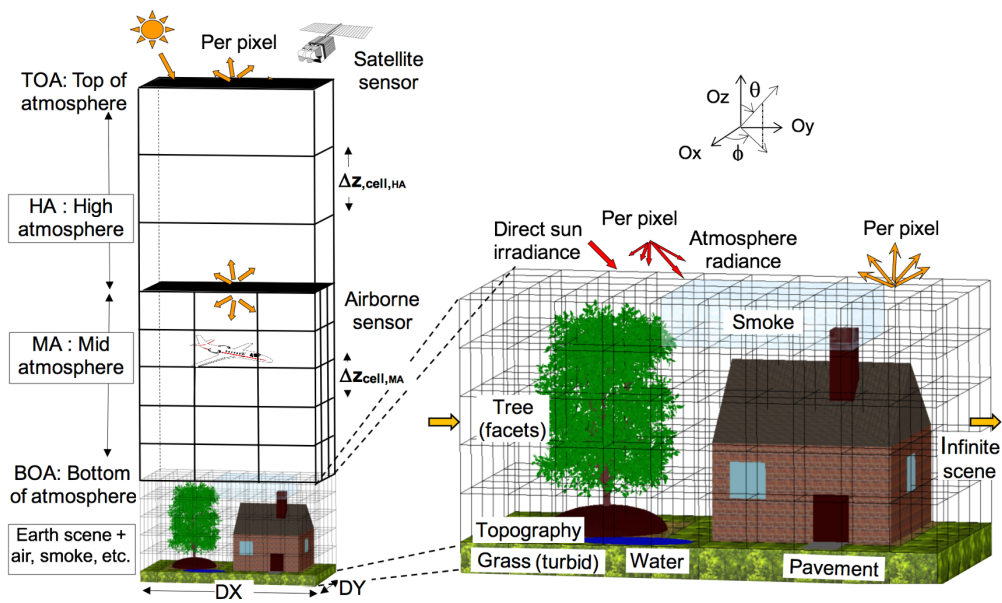
98 the high resolution (spectral resolution up to 0.001 cm^{-1}) spectroscopic databases, such as
99 HITRAN and GEISA (Jacquinet-Husson et al., 2016; Rothman et al., 2009). These models
100 compute the absorption transmittance with either the exact gas absorption cross-section lines
101 (line-by-line models like 4A/OP) or the statistically determined gas absorption cross-section
102 lines (band models like MODTRAN). Therefore, their absorption transmittance is usually more
103 accurate than the absorption transmittance calculated with Beer's law and band mean absorption
104 cross-sections. In addition, the thermal emission of an atmosphere layer computed with the
105 layer mean temperature is incorrect if the layer is optically thick. MODTRAN improved it by
106 computing the layer thermal emission with the "linear-in-optical depth" method (Clough et al.,
107 1992).

108
109 This paper presents two major improvements of DART TIR RT modelling in order to meet the
110 requirements of LST applications and TIR EO satellite missions: (1) introduction of the
111 pressure- and temperature-dependent equivalent absorption cross-section of five most
112 absorbing gases (H_2O , CO_2 , O_3 , CH_4 , N_2O); (2) implementation of an efficient double-layer
113 thermal emission method that is adapted to most atmospheric conditions. Limits of these two
114 improvements are also discussed. Then, the improved DART is compared with MODTRAN-5
115 using standard atmosphere profiles and the actual atmosphere profiles from ECMWF reanalysis
116 dataset.

118 **2. DART model**

119
120 DART (<https://dart.omp.eu>) has been developed at CESBIO since 1992 (Gastellu-Etchegorry
121 et al., 2017, 1996). It is one of the most accurate and comprehensive 3D RT models for the
122 remote sensing community. It simulates the radiative budget, bi-directional reflectance factor

123 (BRF) and images at any altitude and along any viewing direction for 3D natural and urban
 124 scenes, with topography and atmosphere (Figure 1), from visible to thermal infrared region. For
 125 that, it uses an iterative discrete ordinate method (DOM) that tracks radiation fluxes along a
 126 finite number of discrete directions. It also simulates terrestrial and aero-spatial LiDAR signal
 127 (point cloud, waveform, photon counting) with an approach that combines Monte Carlo method
 128 and DOM.



129

130 Figure 1. DART 3D mock-up and voxel matrix. Atmosphere is separated in three altitude regions: high
 131 atmosphere (HA) made of layers, mid-atmosphere (MA) made of voxels of any size, and
 132 bottom atmosphere (BA) in the Earth scene. Earth scene elements are made of facets
 133 (triangles), and/or fluid and turbid vegetation voxels. The voxel matrix is introduced to
 134 optimize ray tracing.

135

136 2.1 DART atmosphere profiles

137

138 DART simulates the atmosphere as three superimposed volumes: (1) bottom atmosphere (BA)
 139 inside the Earth scene voxel matrix, (2) mid-atmosphere (MA) made of voxels, and (3) high

140 atmosphere (HA) made of layers (Figure 1). The geometry of MA and HA (*i.e.*, number of
141 layers, layer thickness, voxel size) is either user-defined or analytically computed. The
142 geometry of BA is the same as the Earth scene. The DART atmosphere SQL database stores
143 vertical profiles of atmospheric constituents (*i.e.*, temperature $T_{DB}(z)$, pressure $P_{DB}(z)$,
144 number density $N_{m_i,DB}(z)$ per gas m_i , relative density $\rho_{m_i,DB}^s(z)$ of scattering gases to air at
145 standard temperature and pressure and aerosol extinction coefficient profile $\alpha_{p,DB}^e(z)$ at 550
146 nm). These profiles are stored at 36 altitude levels (0 to 25 km with 1 km interval, 30 to 60 km
147 with 5 km interval and 3 levels at 70 km, 80 km and 100 km) for:

- 148 - six standard atmospheres (Anderson et al., 1986): (1) TROPICAL: Tropical (15°N annual
149 average), (2) MIDLATSUM: Mid-Latitude Summer (45°N July), (3) MIDLATWIN: Mid-
150 Latitude Winter (45°N January), (4) SUBARCSUM: Sub-Arctic Summer (60°N July), (5)
151 SUBARCWIN: Sub-Arctic Winter (60°N January), and (6) USSTD76: US Standard 1976.
- 152 - five aerosol models (Shettle and Fenn, 1979): (1) Rural, (2) Urban, (3) Maritime, (4)
153 Tropospheric and (5) Fog.

154

155 The DART atmosphere SQL database also stores the spectral optical properties of atmospheric
156 constituents (*i.e.*, gas: vertical absorption transmittance $t_{m_i,DB}^a(\lambda)$ per gas m_i , vertical
157 scattering transmittance $t_{m_i,DB}^s(\lambda)$; aerosol: vertical optical depth $\tau_{p,DB}(\lambda)$, single scattering
158 albedo $\omega_{p,DB}(\lambda)$, asymmetry factors of double Henyey-Greenstein phase function) from 10 to
159 40000 cm^{-1} with a spectral resolution of 1 cm^{-1} . They were derived from MODTRAN
160 simulations and LOWTRAN source code for the six standard atmospheres and for the five
161 aerosol models per standard atmosphere. The optical properties and vertical profiles of gases
162 and aerosols derived from reanalysis datasets (*e.g.*, ECMWF reanalysis: <https://www.ecmwf.int>)
163 and measurements (*e.g.*, Aeronet: <https://aeronet.gsfc.nasa.gov>) can also be imported into the
164 DART atmosphere database.

165

166 The atmosphere properties at any altitude z are interpolated by the multi-quadric RBF (Radial
 167 Basis Function) (Press et al., 2007) using vertical profiles and optical properties in the SQL
 168 database. The band (central wavelength λ , bandwidth $\Delta\lambda$) mean optical properties (*i.e.*, vertical
 169 absorption transmittance $t_{m_i}^a(\lambda)$ of each gas m_i , gas vertical scattering transmittance $t_m^s(\lambda)$,
 170 aerosol vertical optical depth $\tau_p(\lambda)$) are computed (trapezoidal integration) using the database
 171 spectral vertical transmittance $t_{m_i,DB}^a(\lambda')$, $t_{m,DB}^s(\lambda')$ and optical depth $\tau_{p,DB}(\lambda')$ at 1 cm^{-1}
 172 spectral resolution in the spectral bin $\Delta\lambda$:

$$t_{m_i}^a(\lambda) = \frac{\int_{\lambda-\Delta\lambda/2}^{\lambda+\Delta\lambda/2} t_{m_i,DB}^a(\lambda') d\lambda'}{\Delta\lambda}, \quad t_m^s(\lambda) = \frac{\int_{\lambda-\Delta\lambda/2}^{\lambda+\Delta\lambda/2} t_{m,DB}^s(\lambda') d\lambda'}{\Delta\lambda} \quad (1)$$

$$\tau_p(\lambda) = \frac{\int_{\lambda-\Delta\lambda/2}^{\lambda+\Delta\lambda/2} \tau_{p,DB}(\lambda') d\lambda'}{\Delta\lambda}$$

173

174 In DART flux tracking mode, the extinction coefficient α (*i.e.*, total α^e , absorption α^a and
 175 scattering α^s extinction coefficient) are constant values per layer j such that their use with
 176 Beer's law gives the band vertical transmittance and optical depth computed in Eq. (1).

$$\alpha_{j,m_i}^a(\lambda) = \frac{-\ln(t_{m_i}^a(\lambda))}{z_j - z_{j-1}} \cdot \frac{\int_{z_{j-1}}^{z_j} \sigma_{m_i}^a(\lambda) \cdot N_{m_i,DB}(z) dz}{\int_0^\infty \sigma_{m_i}^a(\lambda) \cdot N_{m_i,DB}(z) dz}$$

$$\alpha_{j,m}^s(\lambda) = \frac{-\ln(t_m^s(\lambda))}{z_j - z_{j-1}} \cdot \frac{\int_{z_{j-1}}^{z_j} \sigma_m^s(\lambda) \cdot N_m^s(z) dz}{\int_0^\infty \sigma_m^s(\lambda) \cdot N_m^s(z) dz} = \frac{-\ln(t_m^s(\lambda))}{z_j - z_{j-1}} \cdot \frac{\int_{z_{j-1}}^{z_j} \rho_{m,DB}^s(z) dz}{\int_0^\infty \rho_{m,DB}^s(z) dz} \quad (2)$$

$$\alpha_{j,p}^e(\lambda) = \frac{\tau_{p,DB}(\lambda)}{z_j - z_{j-1}} \cdot \frac{\int_{z_{j-1}}^{z_j} \alpha_{p,DB}^e(z) dz}{\int_0^\infty \alpha_{p,DB}^e(z) dz}$$

177

178 The Newton-Cotes integration method is used in Eq. (2) with 10 interpolated equal-distance
 179 values per layer (Abramowitz and Stegun, 1948) assuming that the absorption cross-section

180 $\sigma_{m_i}^a(\lambda)$ of gas m_i only depends on wavelength. The gas scattering cross-section $\sigma_m^s(\lambda)$ only
 181 depends on wavelength and gas composition (Bodhaine et al., 1999). Therefore, $\sigma_m^s(\lambda) \cdot N_m^s(z)$,
 182 with $N_m^s(z)$ being the number density of scattering gases at altitude z , is proportional to the
 183 relative density of scattering gases $\rho_{m,DB}^s(z)$.

184

185 Then, the total gas extinction coefficient $\alpha_{j,m}^e(\lambda)$, aerosol absorption $\alpha_{j,p}^a(\lambda)$ and scattering
 186 $\alpha_{j,p}^s(\lambda)$ extinction coefficient and total extinction coefficient $\alpha_j^e(\lambda)$ are computed per layer:

$$\alpha_{j,m}^e(\lambda) = \alpha_{j,m}^a(\lambda) + \alpha_{j,m}^s(\lambda), \alpha_{j,m}^a(\lambda) = \sum_{m_i} \alpha_{j,m_i}^a(\lambda)$$

$$\alpha_{j,p}^a(\lambda) = \alpha_{j,p}^e(\lambda) \cdot (1 - \omega_{p,DB}(\lambda)), \alpha_{j,p}^s(\lambda) = \alpha_{j,p}^e(\lambda) \cdot \omega_{p,DB}(\lambda) \quad (3)$$

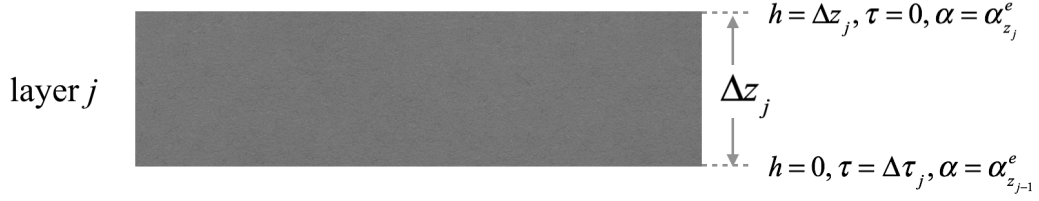
$$\alpha_j^e(\lambda) = \alpha_{j,m}^e(\lambda) + \alpha_{j,p}^e(\lambda)$$

187

188 As explained in section 4, in order to improve the modelling of thermal emission, we adapted
 189 the continuous optical depth profiles per atmosphere layer computed in the DART LiDAR
 190 mode (Gastellu-Etchegorry et al., 2015). Hence, $\alpha_j^e(\lambda, h)$ and $\tau_j(\lambda, h) = \int_0^{\Delta z_j} \alpha_j^e(\lambda, h) dh$ are
 191 continuous functions per atmosphere layer j defined as
 192 $\tau_j(\lambda, h) = A_j(\lambda) \cdot h^3 + B_j(\lambda) \cdot h^2 + C_j(\lambda) \cdot h + D_j(\lambda)$ and $\alpha_j^e(\lambda, h) = -3A_j(\lambda) \cdot h^2 - 2B_j(\lambda) \cdot h - C_j(\lambda)$,
 193 where h is the relative altitude in layer j , with $h=0$ at the bottom of layer j and $h=\Delta z_j$ at the top
 194 of layer j . The verification of the four equalities $\tau(\lambda, 0) = \Delta \tau_j(\lambda)$, $\tau(\lambda, \Delta z_j) = 0$,
 195 $\alpha_j^e(\lambda, 0) = \alpha_{z_{j-1}}^e(\lambda)$, $\alpha_j^e(\lambda, \Delta z_j) = \alpha_{z_j}^e(\lambda)$ derives the coefficients $A_j(\lambda)$, $B_j(\lambda)$, $C_j(\lambda)$ and $D_j(\lambda)$
 196 (Eq. (4)).

$$A_j(\lambda) = \frac{2\Delta \tau_j(\lambda) - (\alpha_{z_{j-1}}^e(\lambda) + \alpha_{z_j}^e(\lambda)) \Delta z_j}{\Delta z_j^3}, B_j(\lambda) = \frac{-3A_j(\lambda) \Delta z_j^2 + \alpha_{z_{j-1}}^e(\lambda) - \alpha_{z_j}^e(\lambda)}{2\Delta z_j} \quad (4)$$

$$C_j(\lambda) = -\alpha_{z_{j-1}}^e(\lambda), D_j(\lambda) = \Delta\tau_j(\lambda)$$



197

198 Figure 2. DART horizontally homogeneous atmosphere layer with layer thickness Δz_j . The upper and
 199 lower boundary parameters are marked.

200

201 2.2 Layer thermal emission

202

203 Thermal emitted vector source (Eq. (5)) of a DART atmosphere layer j (horizontal surface ΔS ,
 204 thickness Δz_j) per direction vector $\Omega(\Delta\Omega)$ (zenith angle θ , azimuth angle φ) is computed using

205 layer mean temperature T_j and two optical properties: single scattering albedo $\omega_j(\lambda) = \frac{\alpha_j^s(\lambda)}{\alpha_j^e(\lambda)}$ and

206 extinction coefficient $\alpha_j^e(\lambda) = \alpha_j^a(\lambda) + \alpha_j^s(\lambda)$, with $\alpha_j^a(\lambda) = \alpha_{j,m}^a(\lambda) + \alpha_{j,p}^a(\lambda)$ the total

207 absorption extinction coefficient and $\alpha_j^s(\lambda) = \alpha_{j,m}^s(\lambda) + \alpha_{j,p}^s(\lambda)$ the total scattering extinction

208 coefficient.

$$\begin{aligned}
 W_j(\Omega, \lambda) &= \int_0^{\Delta z_j} L_B(T_j, \lambda) \cdot \alpha_j^a(\lambda) \cdot \Delta S \cdot \Delta\Omega \cdot e^{-\int_z^{\Delta z_j} \alpha_j^e(\lambda) \frac{dz}{\mu}} dz \\
 &= (1 - \omega_j(\lambda)) \cdot L_B(T_j, \lambda) \cdot \left[1 - e^{-\frac{\Delta\tau_j}{\mu}} \right] \cdot \mu \cdot \Delta S \cdot \Delta\Omega
 \end{aligned}
 \tag{5}$$

209 where $L_B(T_j, \lambda)$ (unit: $W/m^2/sr/\mu m$) is the spectrally averaged Planck function at layer mean

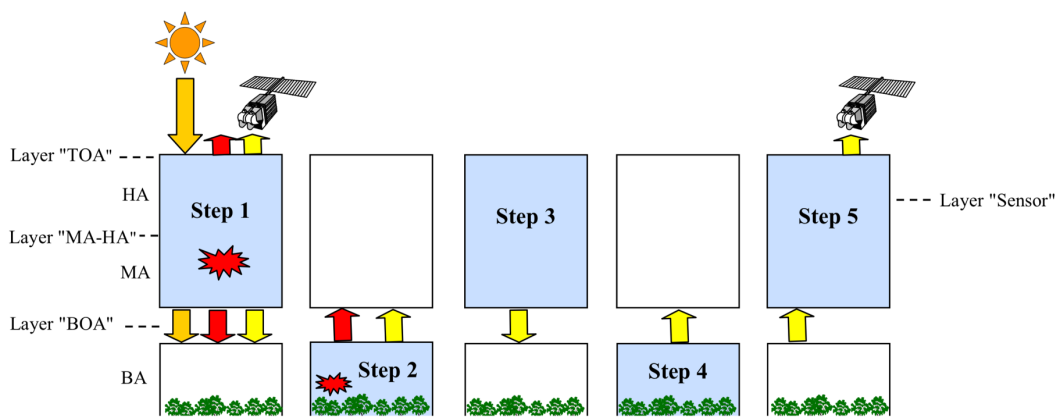
210 temperature T_j . $\Delta\tau_j$ is the optical depth of the atmosphere layer j . $\mu = \cos(\theta)$.

211

212 **2.3 RT in the Earth-atmosphere system**

213

214 RT modelling in the Earth-atmosphere system involves five major steps (Figure 3): (1) Sun
215 illumination and atmosphere thermal emission; (2) Earth surface RT; (3) Earth-atmosphere
216 radiative coupling and atmosphere backscattering; (4) Earth surface RT of the backscattered
217 radiation; (5) Transfer of bottom of atmosphere (BOA) radiation to any altitude, including TOA
218 (Grau and Gastellu-Etchegorry, 2013).



219

220 Figure 3. Major steps for modelling the RT in the Earth-atmosphere system. Red colour indicates
221 thermal emission (steps 1 and 2), orange colour indicates solar incident radiation, and yellow
222 colour indicates thermal and/or solar radiation that is scattered.

223

224 **3. Initial DART atmospheric RT modelling accuracy**

225

226 DART atmospheric RT modelling accuracy was assessed using MODTRAN-5 since it is one
227 of the most accurate atmospheric RT models, with transmittance accuracy ± 0.005 , radiance
228 accuracy $\pm 2\%$ and thermal brightness temperature (BT) accuracy better than 1 K (Berk et al.,
229 2008, 2005, 1987). In the short waves (*i.e.*, $[0.4 \mu\text{m}, 3.0 \mu\text{m}]$), with ground albedo 0.5, TOA
230 nadir reflectance absolute difference between DART and MODTRAN-5 was less than 0.004,

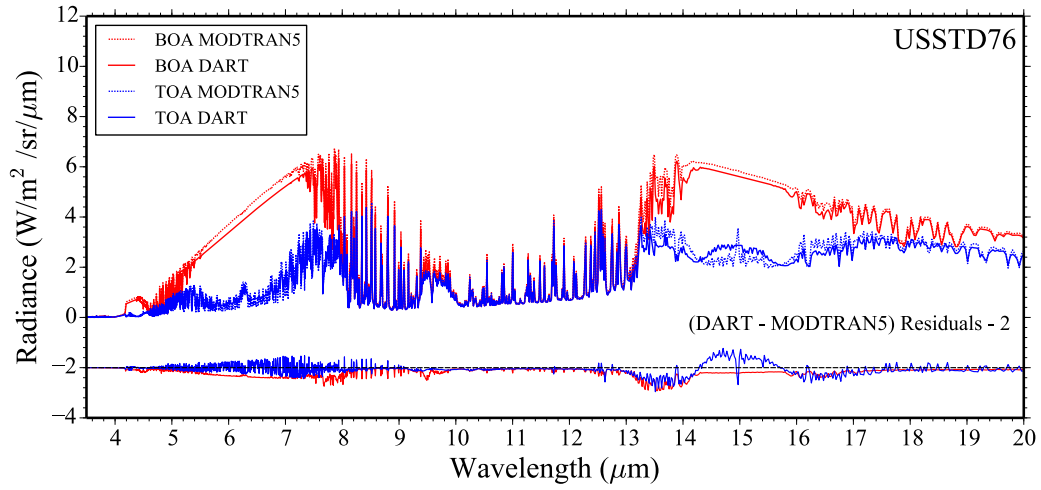
231 which meets MODTRAN-5 accuracy (Gastellu-Etchegorry et al., 2017; Grau and Gastellu-
 232 Etchegorry, 2013). Here, the comparison is extended to TIR region from 3.5 μm to 20 μm ,
 233 using DART version 5.7.3, hereafter called "initial DART". To analyse pure gas atmosphere
 234 emission, MODTRAN-5 and DART were run with thermal emission mode, no aerosol, the
 235 Earth skin temperature is 0 K, surface albedo is 0, and the atmosphere layer depth is equal to 1
 236 km from 0 to 25 km, and 5 km from 30 km to 100 km. Figure 4 shows DART and MODTRAN-
 237 5 TOA and BOA TIR radiance spectra and the residuals, for four standard atmospheres
 238 (USSTD76, TROPICAL, MIDLATSUM, SUBARCWIN). The mean absolute error (MAE)
 239 and mean absolute relative error (MARE) instead of the root-mean-square-error (RMSE) are
 240 used to quantify DART and MODTRAN-5 differences since they bring a more unambiguous
 241 information (Willmott and Matsuura, 2005). For a variable $X(q)$ (e.g., BT, radiance) at band q
 242 and Q spectral bands:

$$\text{MAE} = \frac{1}{Q} \cdot \sum_{q=1}^Q |X_{\text{DART}}(q) - X_{\text{MODTRAN5}}(q)| \quad (6)$$

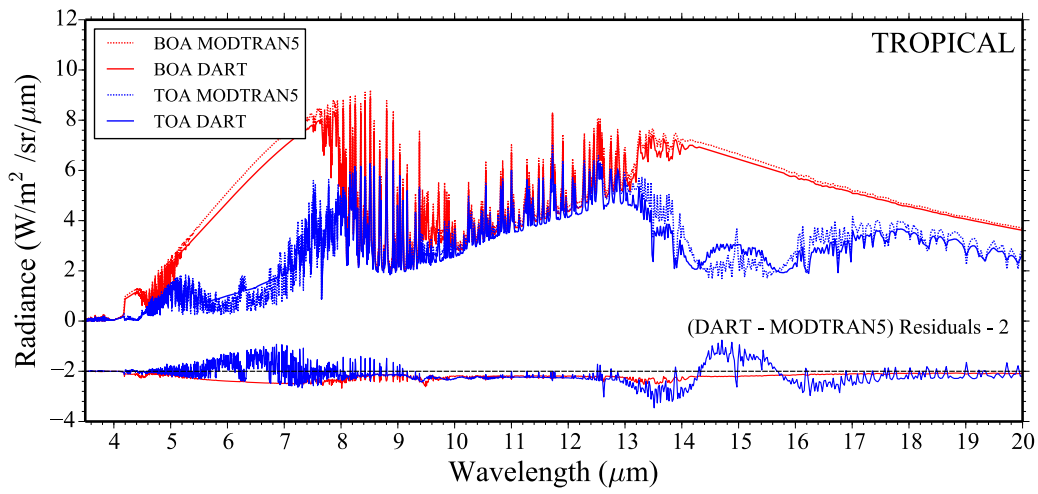
$$\text{MARE} = \frac{1}{Q} \cdot \sum_{q=1}^Q \frac{|X_{\text{DART}}(q) - X_{\text{MODTRAN5}}(q)|}{X_{\text{MODTRAN5}}(q)} \cdot 100 \%$$

243

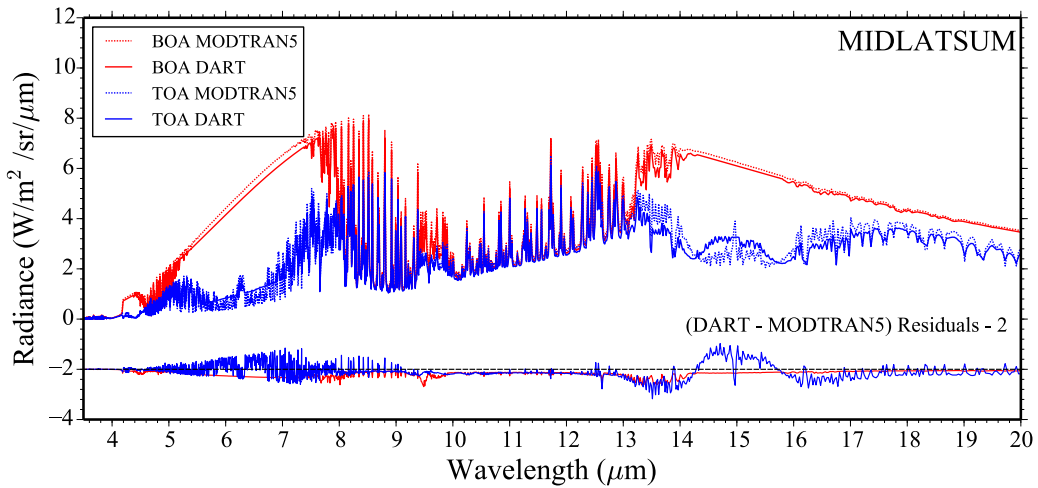
244 Note that the error defined in Eq. (6) is relative to MODTRAN, one should take into account
 245 the accuracy of MODTRAN in practical application.



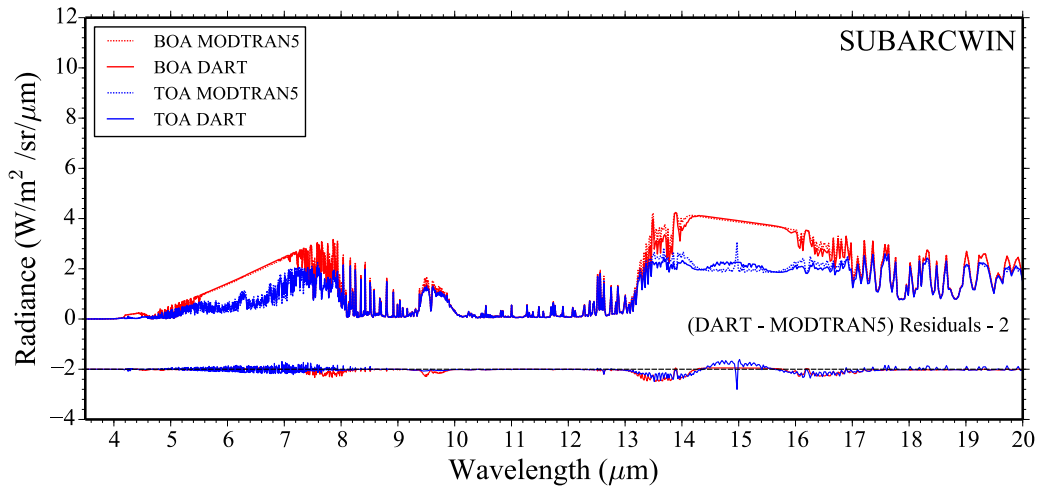
a)



b)



c)



d)

246 Figure 4. Initial DART and MODTRAN-5 TOA / BOA TIR radiance in $[3.5 \mu\text{m}, 20 \mu\text{m}]$ region for
 247 USSTD76 (a), TROPICAL (b), MIDLATSUM (c) and SUBARCWIN (d) atmospheres. 1
 248 cm^{-1} spectral resolution. DART and MODTRAN-5 configurations are detailed in section 3.

249

250 Table 1 summarizes the "Initial DART - MODTRAN-5" MAEs for BT and MAREs for
 251 radiance, for six standard atmospheres. For most standard atmospheres, BT MAEs are larger
 252 than 2.0 K and 1.5 K for TOA and BOA radiance spectra, respectively. The maximal BT MAE
 253 occur for the TROPICAL atmosphere at TOA level with Max (BT MAE) = 4.7 K.

254

255 Table 1. TOA and BOA BT MAE and radiance MARE of initial DART in $[3.5 \mu\text{m}, 20 \mu\text{m}]$ region for
 256 six standard atmospheres. MODTRAN-5 results are the reference.

Atmosphere	BT MAE		Radiance MARE	
	TOA (K)	BOA (K)	TOA (%)	BOA (%)
USSTD76	3.1 K	2.7 K	12.6	8.6
TROPICAL	4.7 K	2.4 K	18.9	6.8
MIDLATSUM	3.8 K	2.1 K	15.0	6.1

MIDLATWIN	2.3 K	1.8 K	10.1	6.3
SUMARCSUM	2.9 K	2.3 K	11.5	7.1
SUMARCWIN	1.8 K	1.3 K	8.0	5.2
Average	3.1 K	2.1 K	12.7	6.7

257

258 DART and MODTRAN-5 TOA / BOA radiance values diverge more in absorbing spectral
259 regions than in non-absorbing spectral regions. For example, Table 2 shows that very large BT
260 differences, up to 7 K, occur in the four absorbing spectral regions: ABS1 ([3.5 μm , 4.5 μm]),
261 ABS2 ([6 μm , 7 μm]), ABS3 ([9 μm , 10 μm]) and ABS4 ([14 μm , 16 μm]) for the USSTD76
262 atmosphere.

263

264 Table 2. TOA and BOA BT MAE and radiance MARE of initial DART in four TIR absorbing bands
265 (ABS1, ABS2, ABS3, ABS4) for the USSTD76 atmosphere. MODTRAN-5 results are the
266 reference.

267

Absorption band	Central wavelength	Bandwidth	BT MAE		Radiance MARE	
			TOA (K)	BOA (K)	TOA (%)	BOA (%)
ABS1	4.0 μm	1.0 μm	2.0 K	1.7 K	12.7	8.3
ABS2	6.5 μm	1.0 μm	5.4 K	3.0 K	25.1	7.9
ABS3	9.5 μm	1.0 μm	2.2 K	3.5 K	7.7	11.0
ABS4	15.0 μm	2.0 μm	7.0 K	3.4 K	13.8	4.0

268

269 DART accuracy was also analysed in relation to three EO satellite missions (Trishna, Sentinel
270 3, Landsat 8). Table 3 shows the BT difference (DIFF) of their TIR bands, for the USSTD76

271 atmosphere. Band BTs are computed by inverting Planck function using band mean radiance
 272 and band central wavelength. The resulting DART BT DIFFs greatly exceed the satellite sensor
 273 sensitivity (Table 3) and also the accuracy usually required for LST applications (*i.e.*, 1 K).

274
 275 Three already mentioned DART approximations can explain these large differences: (1)
 276 Neglect of gas absorption cross-section dependence on pressure and temperature. Indeed, due
 277 to the Doppler and Lorentz broadening, absorption cross-sections vary with pressure and
 278 temperature, and consequently with altitude; (2) Transmittance computation with Beer's law
 279 and band mean optical properties. Indeed, Beer's law is less correct if the absorption cross-
 280 section varies strongly within the spectral bin; (3) Computation of layer thermal emission with
 281 the layer mean temperature T_j , which is only suited for optically thin layers. Therefore, with
 282 the objective that DART accuracy meets the requirements of TIR EO satellite missions and
 283 LST applications while using Beer's law, two major modelling improvements have been made:
 284 (1) account of the vertical variation of gas absorption cross-section, and (2) accurate
 285 computation of thermal emission per layer.

286
 287 Table 3. TOA BT DIFF of initial DART in the TIR bands of three EO satellite missions for the
 288 USSTD76 atmosphere. MODTRAN-5 results are the reference.

Satellite	Launch date	Organization	Central wavelength	Bandwidth	Sensitivity (NeDT)	DIFF
Trishna	Foreseen	CNES+ISRO	8.6 μm	0.35 μm	0.3 K@300 K	0.65 K
	2024-2025		9.1 μm	0.35 μm	0.3 K@300 K	1.57 K
			10.3 μm	1.0 μm	0.3 K@300 K	2.60 K

			11.5 μm	1.0 μm	0.3 K@300 K	1.50 K
Landsat 8	2013	NASA	10.9 μm	0.6 μm	0.4 K@300 K	1.97 K
			12.0 μm	1.0 μm	0.4 K@300 K	1.73 K
Sentinel 3	2016	ESA	3.74 μm	0.38 μm	0.08 K@270 K	0.10 K
			10.95 μm	0.9 μm	0.05 K@270 K	1.88 K
			12.0 μm	1.0 μm	0.05 K@270 K	1.73 K

289

290 4. Improvement to TIR RT modelling

291 4.1 Equivalent absorption cross-section database

292 4.1.1 Equivalent absorption cross-section

293

294 As stated above, the initial DART neglects the dependence of gas absorption cross-sections
 295 with pressure and temperature. We improved this situation by introducing vertical profiles of
 296 equivalent absorption cross-section $\sigma_{m_i}^a(\lambda, z, \Delta L)$ (Eq. (7)) for five most absorbing gases (H₂O,
 297 CO₂, O₃, CH₄, N₂O). $\sigma_{m_i}^a$ is the exact band mean absorption cross-section if Beer's law is
 298 obeyed.

$$\sigma_{m_i}^a(\lambda, z, \Delta L) = \frac{-\ln\left(t_{m_i}^a(\lambda, z, \Delta L)\right)}{N_{m_i}(z) \cdot \Delta L} \quad (7)$$

299

300 with $t_{m_i}^a(\lambda, z, \Delta L)$ the path absorption transmittance of gas m_i at altitude z , at wavelength λ ,
 301 along path segment ΔL . $N_{m_i}(z)$ is the number density of gas m_i at altitude z .

302

303 To compute $\sigma_{m_i}^a(\lambda, z, \Delta L)$ (Eq. (7)), MODTRAN 1 cm^{-1} resolution absorption transmittances
 304 $t_{m_i}^a(\lambda, z, \Delta L)$ were simulated per gas m_i (H_2O , CO_2 , O_3 , CH_4 , N_2O) for identical horizontal
 305 paths ΔL at 36 altitudes z : 26 altitudes from 0 km up to 25 km with a step of 1 km, 7 altitudes
 306 from 25 km up to 60 km with a step of 5 km, and 3 altitudes at 70 km, 80 km and 100 km. The
 307 gas number density $N_{m_i}(z)$ is derived from MODTRAN tape6 file (Berk et al., 2008).

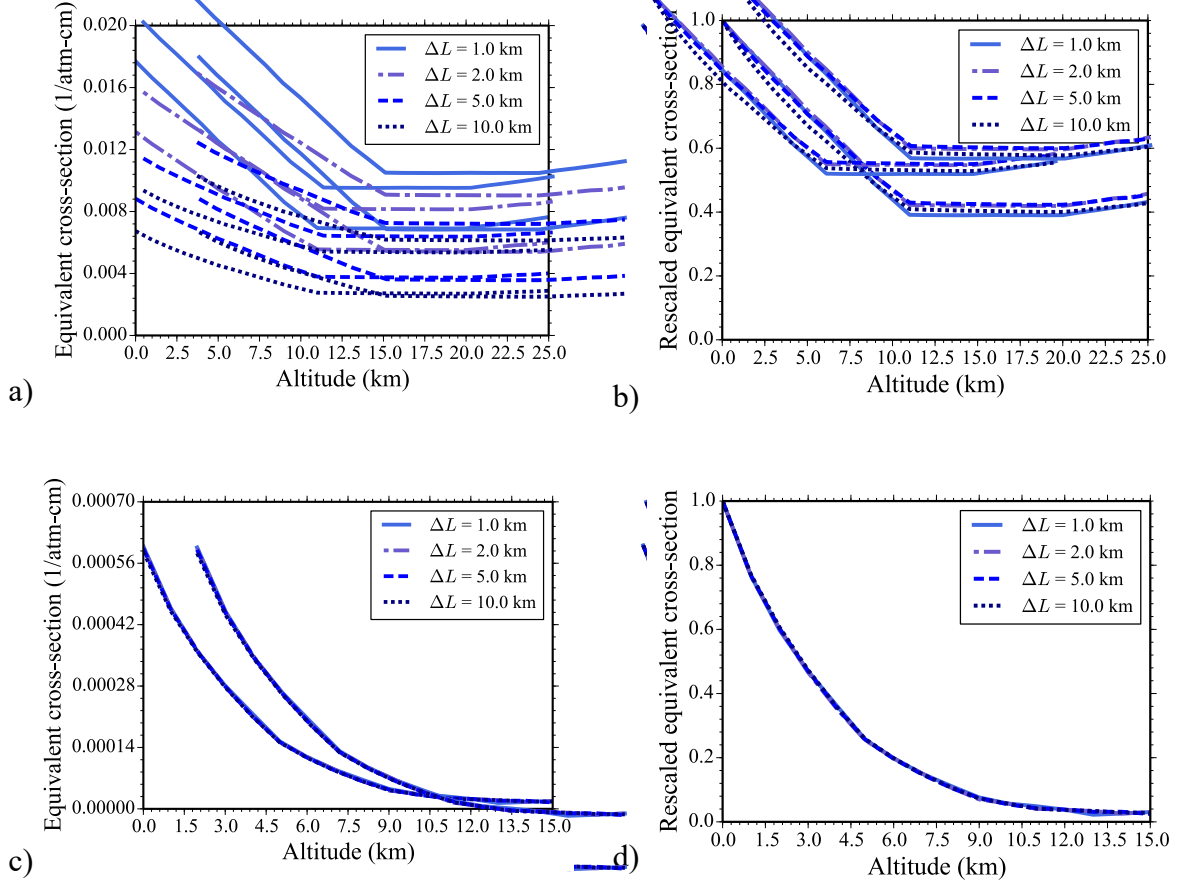
308

309 Figure 5.a and Figure 5.c show the CO_2 vertical profiles of $\sigma_{m_i}^a(\lambda, z, \Delta L)$ from 0 km altitude up
 310 to 25 km for $13.4 \mu\text{m}$ and up to 15 km for $13.1 \mu\text{m}$, with $\Delta L = 1 \text{ km}, 2 \text{ km}, 5 \text{ km}$ and 10 km .
 311 $\sigma_{m_i}^a(\lambda, z, \Delta L)$ profiles depend on ΔL if Beer's law is not obeyed (Figure 5.a) and do not depend
 312 on ΔL if Beer's law is obeyed (Figure 5.c). Figure 5.b, d shows that the relative vertical
 313 distribution of equivalent absorption cross-section $\sigma_{m_i}^{a(*)}(\lambda, z, \Delta L) = \frac{\sigma_{m_i}^a(\lambda, z, \Delta L)}{\sigma_{m_i}^a(\lambda, 0, \Delta L)}$ (profiles scaled
 314 by $\sigma_{m_i}^a(\lambda, 0, \Delta L)$ at $z = 0$) is almost independent of ΔL , even if Beer's law is not obeyed, with
 315 slightly variations depending on the absorption feature, temperature and pressure. It explains
 316 that DART TIR radiance computed with $\sigma_{m_i}^a(\lambda, z, \Delta L)$ only slightly varies with ΔL . Results in
 317 section 5 show that the optimal ΔL is 7 km. Hereafter, $\sigma_{m_i}^a(\lambda, z)$ stands for $\sigma_{m_i}^a(\lambda, z, \Delta L =$
 318 $7 \text{ km})$.

319

320 Note that $\sigma_{m_i}^a(\lambda, z)$ is underestimated if the minus logarithm of total transmittance reaches the
 321 limit 100 in MODTRAN (*i.e.*, extreme absorbing bands). It can occur at low altitude. Then, the
 322 low atmosphere tends to behave as a black body, and the vertical distribution of absorption
 323 extinction coefficient within the low atmosphere has little impact on TIR radiance.

324



325 Figure 5. CO₂ equivalent absorption cross-section $\sigma_{m_i}^a(\lambda, z, \Delta L)$ (a, c) and rescaled equivalent
 326 absorption cross-section $\sigma_{m_i}^{a(*)}(\lambda, z, \Delta L)$ (b, d) at 13.4 μm (a, b) and 13.1 μm (c, d), in 1 cm^{-1}
 327 spectral bin, for 4 identical horizontal paths ($\Delta L = 1 \text{ km}, 2 \text{ km}, 5 \text{ km}, 10 \text{ km}$) at altitudes up
 328 to 25 km for 13.4 μm and up to 15 km for 13.1 μm , in the USSTD76 atmosphere.
 329

330 4.1.2 Creation of SQL database

331

332 The equivalent absorption cross-section profiles $\sigma_{m_i}^a(\lambda, z)$ were computed per gas m_i for the
 333 six standard atmospheres, from 10 to 3500 cm^{-1} at 1 cm^{-1} spectral resolution. To ease data access
 334 and management, they were stored in a SQL database per spectral band, per gas m_i and per
 335 standard atmosphere. Three criteria were used to select the spectral bands of interest: (1)
 336 wavelength larger than 3 μm ; (2) absorbing gases; (3) absorbing spectral regions.

337

338 The spectral region over 3 μm is chosen because the vertical variation of absorption cross-
339 section impacts much more the TIR region than short waves. Also, since non-absorbing gases
340 have a negligible impact on the TOA / BOA radiance, $\sigma_{m_i}^a(\lambda, z)$ is stored only for the five most
341 absorbing gases (H_2O , CO_2 , O_3 , CH_4 , N_2O) and for the absorbing spectral regions of these gases.
342 This trade-off allows one to get accurate TIR RT modelling without increasing too much the
343 DART code complexity and computer time. In non-absorbing bands, MODTRAN absorption
344 transmittance $t_{m_i}^a(\lambda, z)$ of gas m_i at any altitude z along the horizontal path is very close to 1
345 (e.g., 0.99995), which implies that the computed equivalent absorption cross-section is either
346 zero or inaccurate. Therefore, we selected absorbing regions per gas m_i . For that, a specific
347 altitude $Z_{m_i}^*$ is defined per gas m_i such that under this altitude over 98% of gas m_i is present.
348 $Z_{\text{H}_2\text{O}}^*$ is 8 km, $Z_{\text{CO}_2}^*$ is 25 km, $Z_{\text{O}_3}^*$ is 40 km, $Z_{\text{CH}_4}^*$ and $Z_{\text{N}_2\text{O}}^*$ are both 23 km. If the sum of
349 equivalent optical depth $-\ln(t_{m_i}^a(\lambda, z))$ for altitude $z > Z_{m_i}^*$ is not negligible (Eq. (8)), the
350 spectral band is considered as an absorbing band for gas m_i , and the $\sigma_{m_i}^a(\lambda, z)$ profile is stored.

$$\sum_{z > Z_{m_i}^*} -\ln(t_{m_i}^a(\lambda, z)) > \varepsilon \quad (8)$$

351

352 where the threshold ε corresponds to MODTRAN precision. Any line-of-sight with equivalent
353 optical depth $-\ln(t_{m_i}^a(\lambda, z))$ smaller than ε is considered as transparent.

354

355 **4.1.3 Improved absorption extinction coefficient profile**

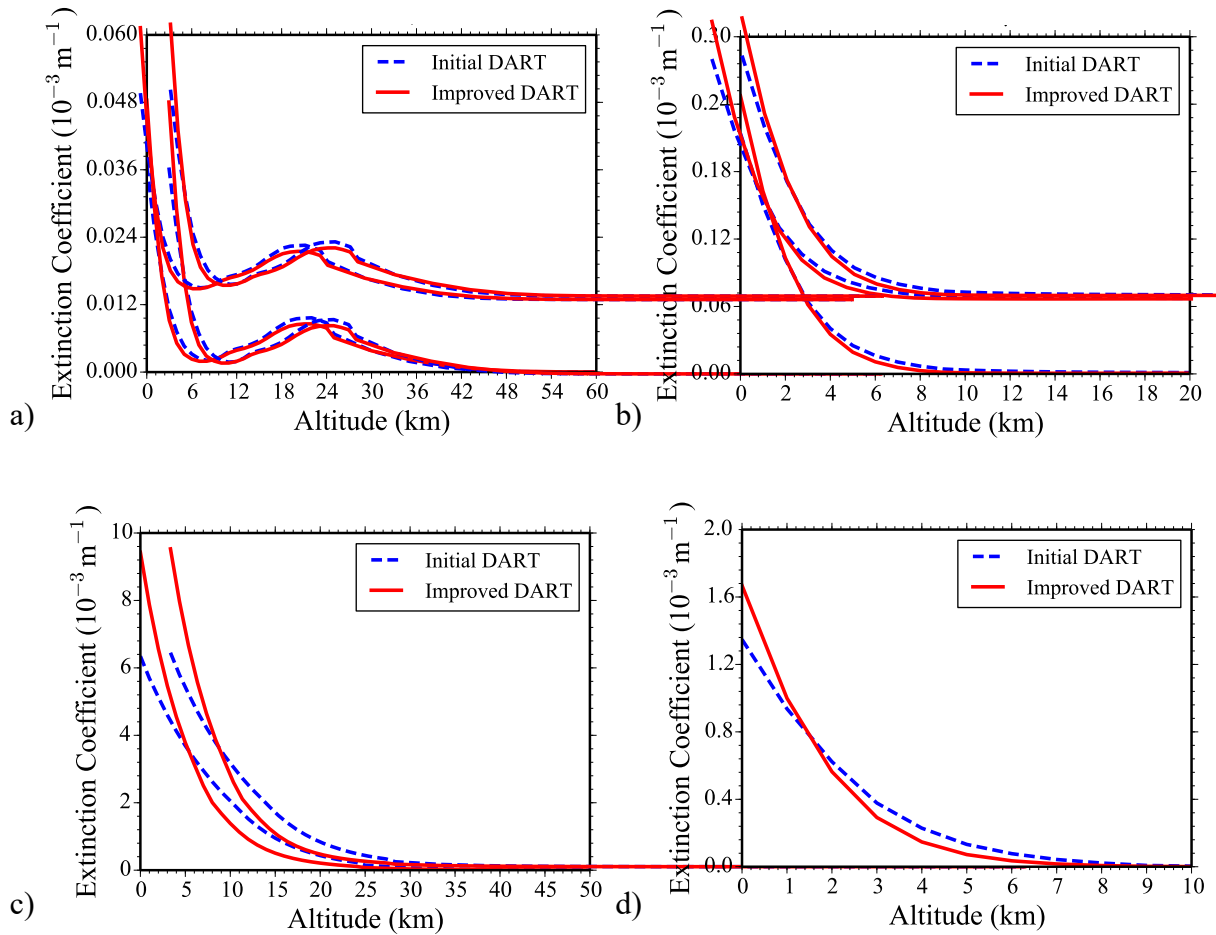
356

357 Eq. (9) indicates how the initial gas absorption extinction coefficient Eq. (2) was improved
358 using the pressure- and temperature-dependent equivalent absorption cross-section.

$$\alpha_{j,m_i}^a(\lambda) = \begin{cases} \frac{-\ln(t_{m_i}^a(\lambda))}{z_j - z_{j-1}} \cdot \frac{\int_{z_{j-1}}^{z_j} \sigma_{m_i}^a(\lambda, z) \cdot N_{m_i,DB}(z) dz}{\int_0^\infty \sigma_{m_i}^a(\lambda, z) \cdot N_{m_i,DB}(z) dz}, & m_i = \text{H}_2\text{O}, \text{CO}_2, \text{O}_3, \text{CH}_3, \text{N}_2\text{O} \\ \frac{-\ln(t_{m_i}^a(\lambda))}{z_j - z_{j-1}} \cdot \frac{\int_{z_{j-1}}^{z_j} \sigma_{m_i}^a(\lambda) \cdot N_{m_i,DB}(z) dz}{\int_0^\infty \sigma_{m_i}^a(\lambda) \cdot N_{m_i,DB}(z) dz}, & m_i \neq \text{H}_2\text{O}, \text{CO}_2, \text{O}_3, \text{CH}_3, \text{N}_2\text{O} \end{cases} \quad (9)$$

359

360 Figure 6 shows vertical profiles of the new absorption extinction coefficients in the USSTD76
 361 atmosphere at four spectral bands. Compared to the initial absorption extinction coefficients,
 362 they tend to be larger at lower altitudes and smaller at higher altitudes. This is consistent with
 363 the stronger absorption behaviour of bottom atmosphere. O₃ absorption explains the local
 364 maximum (≈ 20 km) of the initial and new absorption extinction coefficients at $10 \mu\text{m}$.



365 Figure 6. Profiles of DART initial and improved absorption extinction coefficients in the USSTD76
 366 atmosphere. a) $10.0 \mu\text{m}$. b) $13.0 \mu\text{m}$. c) $15.4 \mu\text{m}$. d) $19.6 \mu\text{m}$. Spectral bin is 1 cm^{-1} .

367

368 4.2 Layer thermal emission

369 4.2.1 A double-layer method

370

371 The initial thermal emission method (Eq. (5)) is less correct for optically thick atmosphere layer

372 (*i.e.*, $\Delta\tau_j \gg 1$). For example, if lower boundary temperature is larger than layer mean

373 temperature and if $\Delta\tau_j \gg 1$, Eq. (5) tends to underestimate downward thermal vector sources

374 $W_j^\downarrow(\Omega, \lambda)$. Hence, a double-layer method was first designed (Eq. (10)): half a layer emits with

375 Planck function $L_B(T_x, \lambda)$, and the other half emits with Planck function $L_B(T_y, \lambda)$.

$$W_j^\uparrow(\Omega, \lambda) = (1 - \omega_j(\lambda)) \cdot \left[L_B(T_x, \lambda) e^{-\frac{\Delta\tau_j}{2\mu}} + L_B(T_y, \lambda) \right] \left[1 - e^{-\frac{\Delta\tau_j}{2\mu}} \right] \cdot \mu \cdot \Delta S \cdot \Delta\Omega \quad (10)$$

$$W_j^\downarrow(\Omega, \lambda) = (1 - \omega_j(\lambda)) \cdot \left[L_B(T_x, \lambda) + L_B(T_y, \lambda) e^{-\frac{\Delta\tau_j}{2\mu}} \right] \left[1 - e^{-\frac{\Delta\tau_j}{2\mu}} \right] \cdot \mu \cdot \Delta S \cdot \Delta\Omega$$

376

377 In order to get T_x and T_y , four equations associated to schematic configurations must be verified:

378 1) Blackbody ($\Delta\tau_j \gg 1$ and $\omega_j(\lambda) \approx 0$)

$$\begin{aligned} W_j^\uparrow(\Omega, \lambda) &= L_B(T_j^U, \lambda) \cdot \mu \cdot \Delta S \cdot \Delta\Omega \\ W_j^\downarrow(\Omega, \lambda) &= L_B(T_j^L, \lambda) \cdot \mu \cdot \Delta S \cdot \Delta\Omega \end{aligned} \quad (11)$$

379

380 with T_j^U and T_j^L respectively the upper and lower boundary temperature of layer j .

381 2) Isothermal ($T_x = T_y = T_j$)

$$W_j^\uparrow(\Omega, \lambda) = (1 - \omega_j(\lambda)) \cdot L_B(T_j, \lambda) \cdot \left[1 - e^{-\frac{\Delta\tau_j}{\mu}} \right] \cdot \mu \cdot \Delta S \cdot \Delta\Omega \quad (12)$$

$$W_j^\downarrow(\Omega, \lambda) = (1 - \omega_j(\lambda)) \cdot L_B(T_j, \lambda) \cdot \left[1 - e^{-\frac{\Delta\tau_j}{\mu}} \right] \cdot \mu \cdot \Delta S \cdot \Delta\Omega$$

382

383 Eq. (11) and (12) lead to $T_x=T_j^L$ and $T_y=T_j^U$. The resulting upward and downward vector
 384 sources are:

$$\begin{aligned} W_j^\uparrow(\Omega, \lambda) &= (1 - \omega_j(\lambda)) \cdot \left[L_B(T_j^L, \lambda) e^{-\frac{\Delta\tau_j}{2\mu}} + L_B(T_j^U, \lambda) \right] \left[1 - e^{-\frac{\Delta\tau_j}{2\mu}} \right] \cdot \mu \cdot \Delta S \cdot \Delta\Omega \\ W_j^\downarrow(\Omega, \lambda) &= (1 - \omega_j(\lambda)) \cdot \left[L_B(T_j^L, \lambda) + L_B(T_j^U, \lambda) e^{-\frac{\Delta\tau_j}{2\mu}} \right] \left[1 - e^{-\frac{\Delta\tau_j}{2\mu}} \right] \cdot \mu \cdot \Delta S \cdot \Delta\Omega \end{aligned} \quad (13)$$

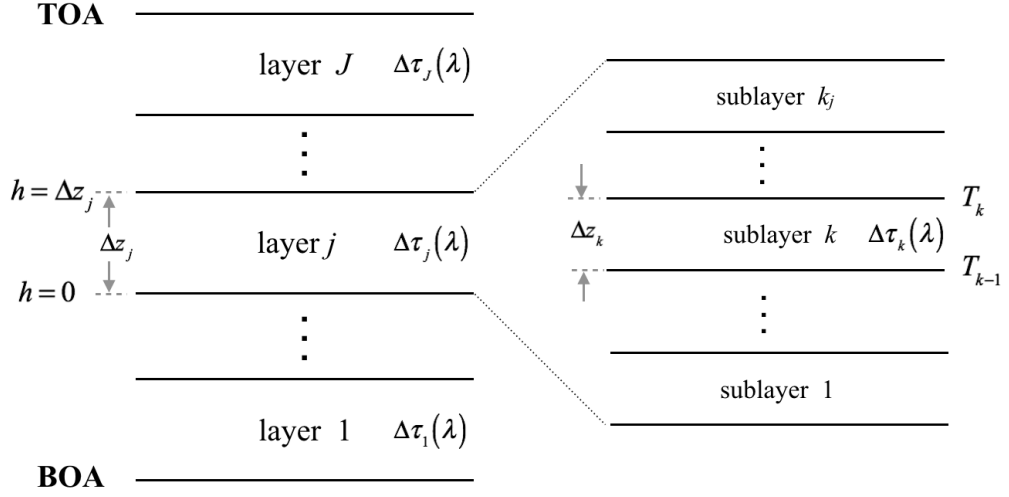
385

386 4.2.2 Thermal emission with virtual sub-layers

387

388 Same as the "linear-in-optical depth" assumption (Clough et al., 1992), the double-layer method
 389 (Eq. (13)) is less correct if the temperature and absorption extinction coefficient gradient within
 390 a layer is large (Wiscombe, 1976). Hence, there is a need to take into account the vertical
 391 distribution of temperature and optical depth in each atmosphere layer. For that, each DART
 392 atmosphere layer j ($j \in [1, J]$, $j = 1$ for the bottom layer) is virtually divided into k_j sub-layers

393 $\Delta\tau_k(\lambda) = \int_{\tau_{k-1}(\lambda)}^{\tau_k(\lambda)} d\tau$ with $k \in [1, k_j]$ (Figure 7). The optical depth of the bottom and top planes
 394 of layer j are noted $\tau_{j-1}(\lambda)$ and $\tau_j(\lambda)$, respectively, with $\tau_j(\lambda) = 0$ and $\tau_{j-1}(\lambda) = \Delta\tau_j(\lambda)$. The
 395 terms $\Delta\tau_k(\lambda)$, $\tau_j(\lambda)$, $\tau_{j-1}(\lambda)$, $\tau_k(\lambda)$ and $\tau_{k-1}(\lambda)$ are computed using analytical expressions of
 396 layer optical depth that was already implemented in DART for LiDAR mode (*i.e.*, $\tau_j(h, \lambda) =$
 397 $A_j(\lambda) \cdot h^3 + B_j(\lambda) \cdot h^2 + C_j(\lambda) \cdot h + D_j(\lambda)$). Temperature profile $T_j(h)$ is written as a linear
 398 approximation: $T_j(h) = T_j^L + \frac{T_j^U - T_j^L}{\Delta z_j} \cdot h$.



399

400 Figure 7. DART atmosphere is made of J layers, with layer optical depth $\Delta\tau_j$ and layer thickness Δz_j .

401 Each layer j is virtually divided into k_j sub-layers, with sub-layer thickness $\Delta z_k = \frac{\Delta z_j}{k_j}$ and
 402 sub-layer optical depth $\Delta\tau_k$, with upper and lower boundary temperature T_k and T_{k-1} ,
 403 respectively.

404

405 The expressions of $W_j^\uparrow(\Omega, \lambda)$ and $W_j^\downarrow(\Omega, \lambda)$ are computed by summing up all contributions of
 406 virtual sub-layer thermal emission using Eq. (13).

$$W_j^\uparrow(\Omega, \lambda) = (1 - \omega_j(\lambda)) \sum_{k=1}^{k_j} \left[L_B(T_{k-1}, \lambda) e^{-\frac{\Delta\tau_k}{2\mu}} + L_B(T_k, \lambda) \right] \left[1 - e^{-\frac{\Delta\tau_k}{2\mu}} \right] e^{-\frac{\tau_k}{\mu}} \cdot \mu \cdot \Delta S \cdot \Delta \Omega \quad (14)$$

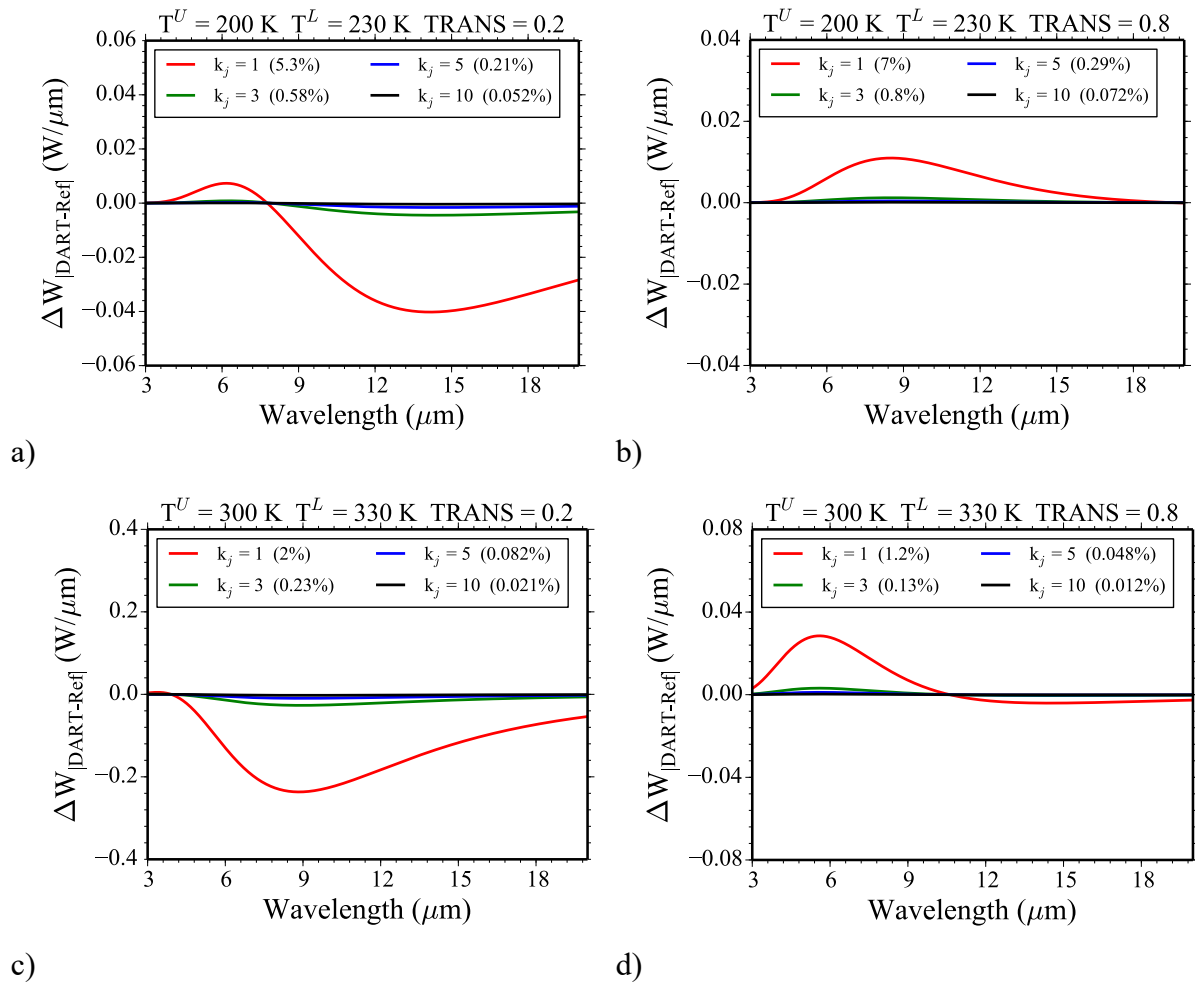
$$W_j^\downarrow(\Omega, \lambda) = (1 - \omega_j(\lambda)) \sum_{k=1}^{k_j} \left[L_B(T_{k-1}, \lambda) + L_B(T_k, \lambda) e^{-\frac{\Delta\tau_k}{2\mu}} \right] \left[1 - e^{-\frac{\Delta\tau_k}{2\mu}} \right] e^{-\frac{(\tau_{j-1} - \tau_{k-1})}{\mu}} \cdot \mu \cdot \Delta S \cdot \Delta \Omega$$

407

408 The optimal number k_j of sub-layers in Eq. (14) was assessed by computing the upward vector
 409 sources ($\omega_j=0$, $\mu=1$, $\Delta S=100 \text{ m}^2$, $\Delta \Omega=0.01 \text{ sr}$) of a hot ($\sim 300 \text{ K}$) and cold ($\sim 200 \text{ K}$) atmosphere
 410 layer ($\Delta z_j=1 \text{ km}$) with small (0.2) and large (0.8) transmittance $e^{-\Delta\tau_j}$, for k_j from 1 to 10, from
 411 $3 \mu\text{m}$ to $20 \mu\text{m}$. Bottom layer parameters are: $T_j^L=T^L$, $\alpha_j^e(0, \lambda)=\alpha_0^e$, $\tau_j(0, \lambda)=\Delta\tau_j$; upper layer
 412 parameters are: $T_j^U=T^U$, $\alpha_j^e(\Delta z_l, \lambda)=\alpha_0^e \cdot e^{-\frac{\Delta z_j}{H}}$, $\tau_j(\Delta z_j, \lambda)=0$, with $H=8.4 \text{ km}$ the usual scale

413 height of major gases. Sub-layer boundary temperature and optical depth are computed as
 414 described at the beginning of this section. Here, the reference is the vector source $W_{\text{ref}}^{\uparrow}(\Omega, \lambda)$
 415 computed with $k_j = 1000$. Figure 8 shows that MARE for $k_j = 1$ can reach 7% and that $k_j = 5$
 416 gives accurate source vectors for most atmospheric conditions. Note that for atmospheric
 417 conditions less extreme than these in this test, the double-layer method usually gives better
 418 results.

419



420 Figure 8. Difference of DART double-layer upward vector source compared with the reference, for
 421 various numbers of sub-layers. T^U and T^L are respectively the upper and lower boundary
 422 temperatures. TRANS represents the layer transmittance. MARE is marked in the legend.

423

424 **5. Results and discussion**

425 **5.1 Results**

426

427 The combined introduction of the equivalent absorption cross-section and double-layer thermal
428 emission method greatly improves the accuracy of DART TIR radiance as illustrated below.

429 **5.1.1 Optimal path length ΔL**

430

431 Section 4 stresses that the path length ΔL used to compute the equivalent absorption cross-
432 section can slightly impact the TIR radiance. Therefore, we investigated 10 equivalent
433 absorption cross-section databases with ΔL from 1 km to 10 km, with 1 km interval, in order to
434 determine the optimal ΔL . TOA and BOA radiance spectra over $[3.5 \mu\text{m}, 20 \mu\text{m}]$ were
435 simulated with these databases for the six standard atmospheres. Table 4 shows the
436 corresponding average MAE of TOA and BOA BT of six standard atmospheres for the
437 equivalent absorption cross-section databases with ΔL from 4 km to 9 km. We chose $\Delta L=7$ km
438 since it gives the best results compared to MODTRAN-5. Note that $\Delta L = 6$ km, 8 km, and 9
439 km can also give good results with average BT MAE less than 0.7 K. Hereafter, all the DART
440 simulations use the " $\Delta L=7$ km" absorption cross-section database.

441

442 Table 4. Average MAE of TOA and BOA BT over $[3.5 \mu\text{m}, 20 \mu\text{m}]$ region of six standard atmospheres,
443 with path lengths ΔL from 4 km to 9 km. MODTRAN-5 results are the reference.

ΔL	4 km	5 km	6 km	7 km	8 km	9 km
AVG BT MAE (K)	0.7489	0.7157	0.6828	0.6728	0.6731	0.6805

444

445 **5.1.2 Improved TOA and BOA thermal radiance**

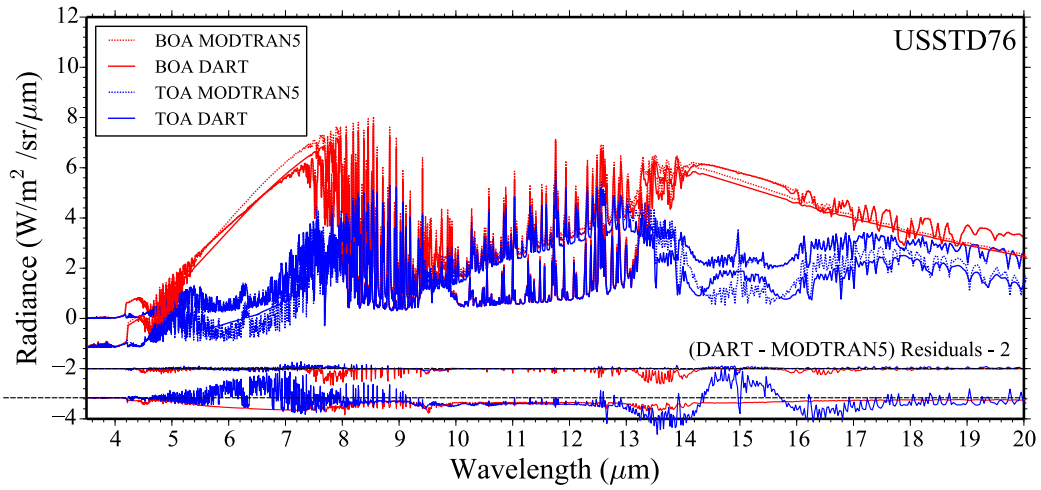
446

447 Figure 9 shows the DART and MODTRAN-5 TIR radiance spectra of the USSTD76,
448 MIDLATSUM, TROPICAL and SUBARCWIN atmospheres, with the same configurations
449 as in Figure 4. Table 5 gives the MAE of TIR BT and MARE of TIR radiance of the improved
450 DART and MODTRAN-5 for the six standard atmospheres over $[3.5 \mu\text{m}, 20 \mu\text{m}]$. Compared
451 to initial results in section 3, the average TIR radiance MARE of the six standard atmospheres
452 is reduced from 12.7% to 3.0% at TOA level, and from 6.7% to 2.3% at BOA level. Similarly,
453 the average BT MAE is reduced from 3.1 K to 0.71 K at TOA level and from 2.1 K to 0.64 K
454 at BOA level. Table 6 indicates that the largest improvements occur in TIR absorbing regions
455 (*e.g.*, 3.5 - 4.5 μm , 6-7 μm , 9-10 μm , 14-16 μm). For example, with the USSTD76 atmosphere,
456 the BT MAE in $[14 \mu\text{m}, 16 \mu\text{m}]$ region is reduced from 7.0 K to 0.9 K at TOA level and from
457 3.4 K to 0.7 K at BOA level.

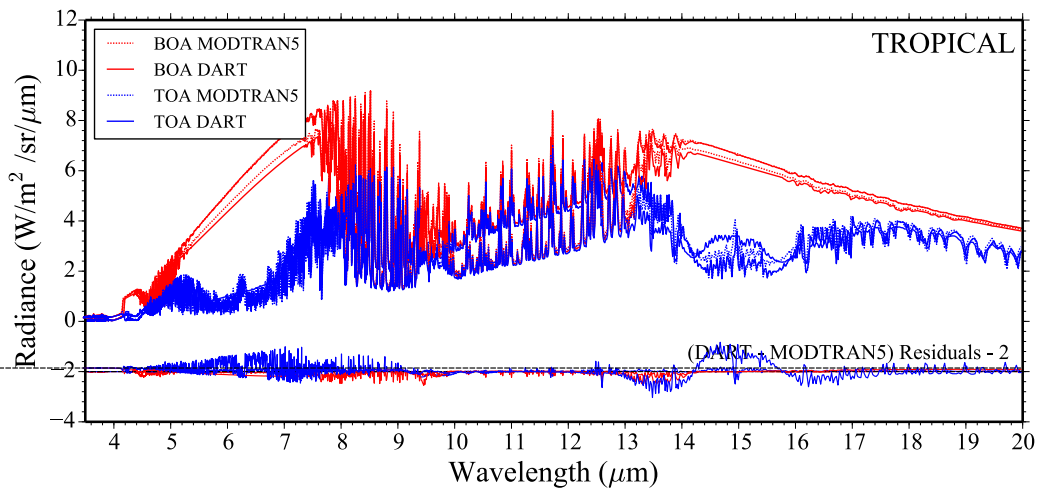
458

459 The BT DIFF "improved DART vs. MODTRAN-5" for the TIR bands of the aforementioned
460 EO satellite missions (Table 7) stresses that current DART accuracy meets the sensitivity of
461 these three satellite missions. For example, for the 12 μm band of Landsat 8, the DIFF is reduced
462 from 1.73 K to 0.025 K, which is much smaller than the sensor sensitivity (0.4 K at 300 K).

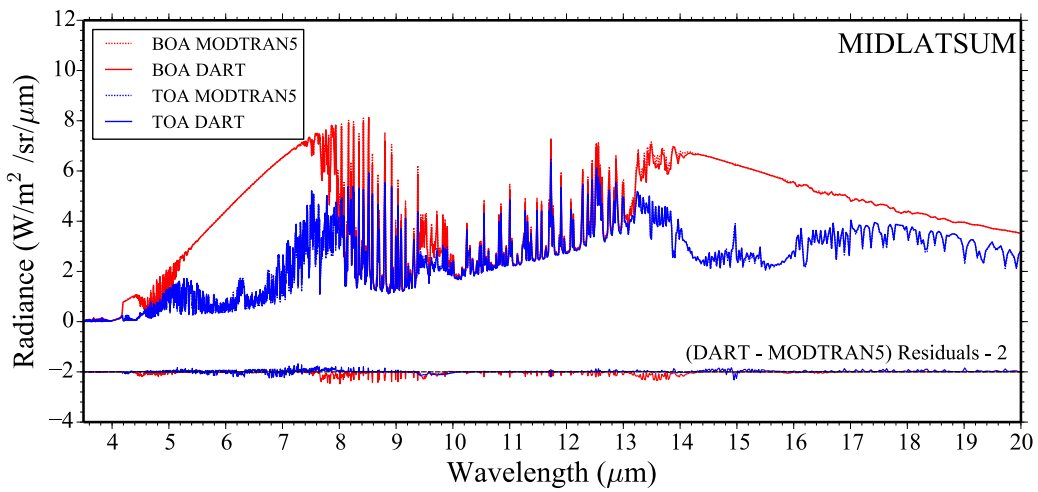
463



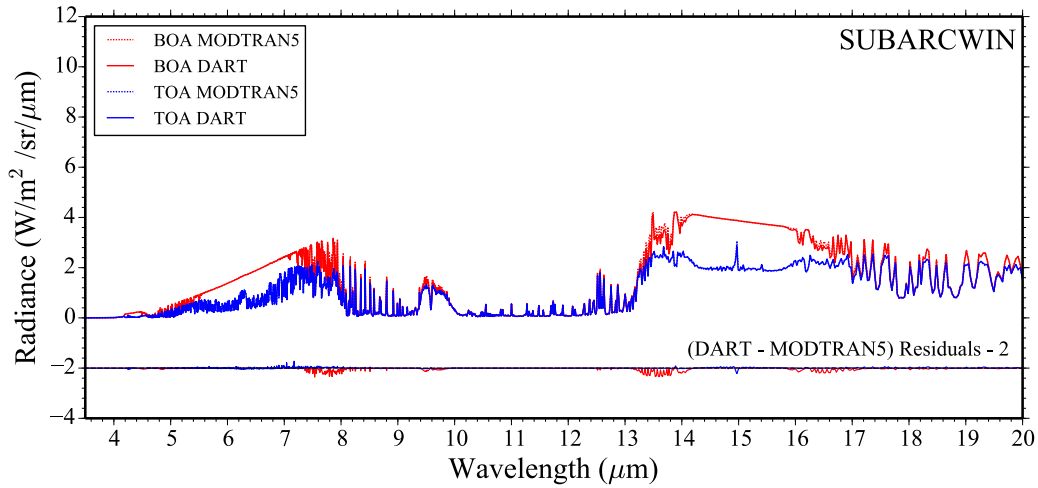
a)



b)



c)



d)

464 Figure 9. Improved DART and MODTRAN-5 TOA / BOA TIR radiance in [3.5 μm , 20 μm] region
 465 for USSTD76 (a), TROPICAL (b), MIDLATSUM (c) and SUBARCWIN (d) atmospheres.
 466 1 cm^{-1} spectral resolution. DART and MODTRAN-5 configurations are detailed in section
 467 3.

468

469 Table 5. TOA and BOA BT MAE and radiance MARE of improved DART in [3.5 μm , 20 μm] region
 470 for six atmospheres. MODTRAN-5 results are the reference.

Atmosphere	TOA MAE	BOA MAE	TOA MARE	BOA MARE
USSTD76	0.68K	0.83K	3.0%	2.8%
TROPICAL	0.97K	0.58K	3.8%	2.0%
MIDLATSUM	0.88K	0.57K	3.5%	2.0%
MIDLATWIN	0.55K	0.63K	2.5%	2.3%
SUMARCWSUM	0.75K	0.66K	3.1%	2.3%
SUMARCWIN	0.44K	0.54K	2.2%	2.2%
AVERAGE	0.71K	0.64K	3.0%	2.3%

471

472 Table 6. TOA and BOA BT MAE and radiance MARE of improved DART in three TIR absorbing
 473 bands for the USSTD76 atmosphere. MODTRAN-5 results are the reference.

Absorption bands	Central wavelength	Bandwidth	TOA MAE	BOA MAE	TOA MARE	BOA MARE
ABS1	4.0 μm	1.0 μm	0.7 K	0.7 K	4.0%	3.5%
ABS2	6.5 μm	1.0 μm	1.4 K	0.1 K	5.5%	0.3%
ABS3	9.5 μm	1.0 μm	0.6 K	1.0 K	1.8%	2.9%
ABS4	15.0 μm	2.0 μm	0.9 K	0.7 K	1.7%	0.9%

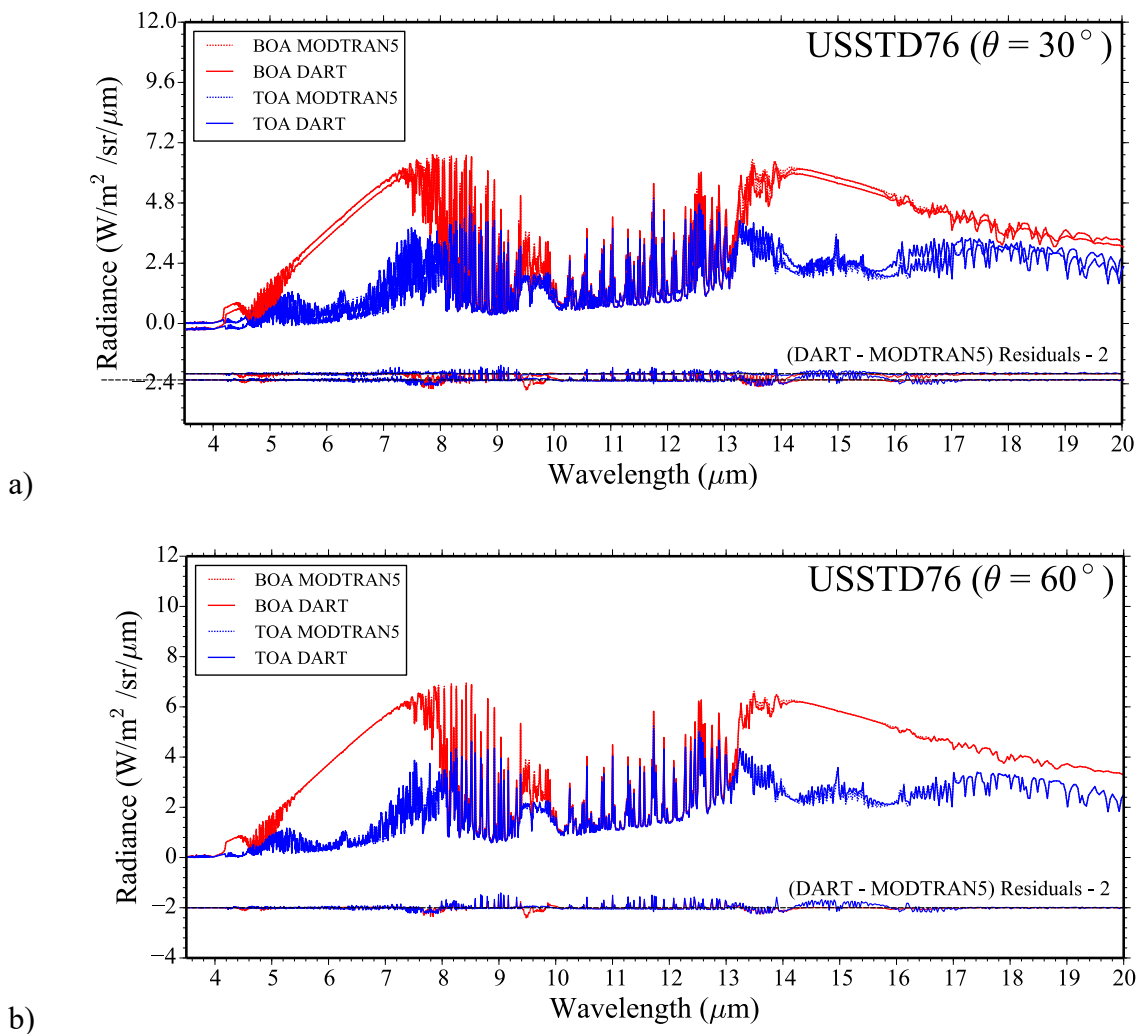
474

475 Table 7. TOA BT DIFF improved DART in the TIR bands of three EO satellite missions for the
 476 USSTD76 atmosphere. MODTRAN-5 results are the reference.

Satellite	Launch date	Organization	Central wavelength	Bandwidth	Sensitivity (NeDT)	Improved DIFF
Trishna	foreseen 2024-2025	CNES+ISRO	8.6 μm	0.35 μm	0.3 K@300 K	0.153 K
			9.1 μm	0.35 μm	0.3 K@300 K	0.049 K
			10.3 μm	1.0 μm	0.3 K@300 K	0.197 K
			11.5 μm	1.0 μm	0.3 K@300 K	0.005 K
Landsat 8	2013	NASA	10.9 μm	0.6 μm	0.4 K@300 K	0.009 K
			12.0 μm	1.0 μm	0.4 K@300 K	0.025 K
Sentinel 3	2016	ESA	3.74 μm	0.38 μm	0.08 K@270 K	0.022 K
			10.95 μm	0.9 μm	0.05 K@270 K	0.011 K
			12.0 μm	1.0 μm	0.05 K@270 K	0.025 K

477

478 The accuracy of the improved DART was successfully tested for oblique viewing directions.
 479 Table 8 summarizes the MAE of TOA and BOA BT for viewing directions with θ from 0° to
 480 60° . Figure 10 shows TOA / BOA TIR radiance spectra for viewing zenith angles $\theta=30^\circ$ and
 481 $\theta=60^\circ$, for the USSTD76 atmosphere. Along viewing zenith angle $\theta=30^\circ$, the BT MAE is
 482 0.74 K at TOA level and 0.70 K at BOA level, along viewing zenith angle $\theta=60^\circ$, the BT MAE
 483 is 1.36 K at TOA level and 0.52 K at BOA level.
 484



485 Figure 10. Improved DART and MODTRAN-5 TOA / BOA TIR radiance in $[3.5 \mu\text{m}, 20 \mu\text{m}]$ region
 486 for the USSTD76 atmosphere. Viewing zenith angle $\theta = 30^\circ$ (a) and $\theta = 60^\circ$ (b).

487 Table 8. Average MAE of TOA and BOA BT of the USSTD76 atmosphere over [3.5 μm , 20 μm]
 488 region, with viewing directions θ from 0° to 60°. MODTRAN-5 results are the reference.

θ	0°	10°	20°	30°	40°	50°	60°
TOA BT MAE (K)	0.68	0.71	0.71	0.74	0.82	1.0	1.36
BOA BT MAE (K)	0.83	0.83	0.78	0.70	0.60	0.53	0.52

489

490 5.2 Validation

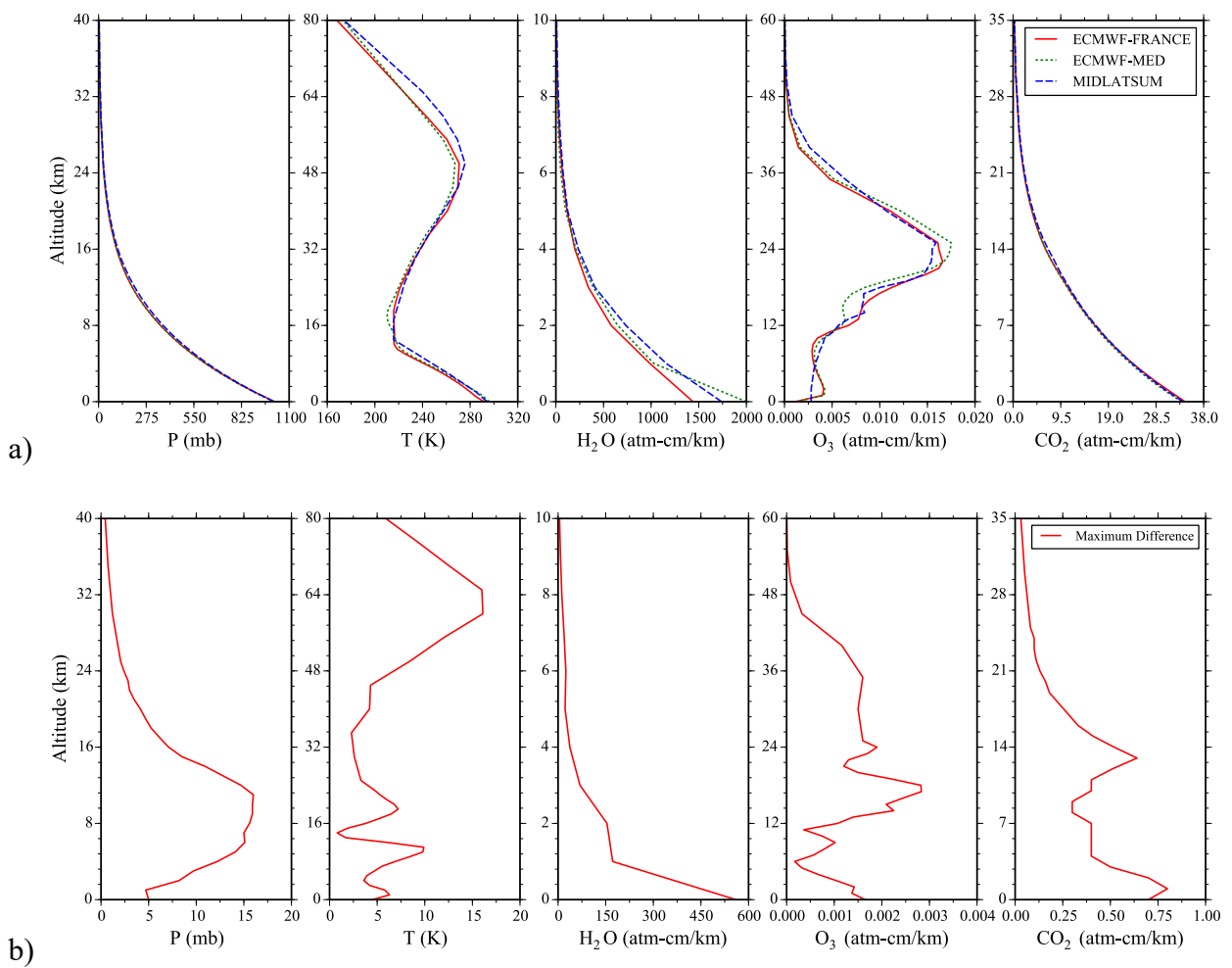
491

492 DART improvement was validated by comparing DART and MODTRAN-5 simulations with
 493 atmosphere profiles from ECMWF (European Centre for Medium-range Weather Forecasts)
 494 reanalysis dataset: ERA-Interim (<https://apps.ecmwf.int/datasets/>). These profiles include the
 495 pressure, temperature, specific humidity (mass of water vapour per kilogram of moist air, nearly
 496 equal to mass mixing ratio within a few percent) and O₃ mass mixing ratio (mass of ozone per
 497 kilogram of dry air) at 60 ECMWF model levels
 498 (<https://www.ecmwf.int/en/forecasts/documentation-and-support/60-model-levels>) as well as
 499 the surface albedo, skin temperature over France (49°N, -1°W, 44°S, 7°E) and the
 500 Mediterranean Sea (37°N,12°W, 34°S, 26°E) from 01/06/2018 to 31/08/2018. These data were
 501 averaged over time and space and the vertical profiles were interpolated into 37 altitude levels
 502 (1 km interval from 0 to 25 km, and 5 km interval from 30 to 80 km) that are configured in both
 503 DART and MODTRAN-5. The number density profile $N_{m_i}(z)$ of other gases (N₂, CO₂, CO,
 504 CH₄, N₂O, O₂, NH₃, NO, NO₂, SO₂, HNO₃, CFC₁₂, CFC₁₃, CFC₁₄, CFC₂₂, CFC₁₁₃, CFC₁₁₄,
 505 CFC₁₁₅, CLONO₂, HNO₄, CHCL₂F, CCL₄, N₂O₅) and the relative density profile $\rho_m^s(z)$ of

506 scattering gases are adjusted by MODTRAN-5 based on the MIDLATSUM atmosphere and
 507 the actual pressure and temperature profile from ERA-Interim dataset.

508

509 Figure 11.a shows the pressure, temperature, H₂O, O₃ and CO₂ number density profiles for three
 510 summer atmospheres in the mid-latitude region: France, Mediterranean Sea, and the standard
 511 MIDLATSUM atmosphere. Figure 11.b shows the corresponding maximum difference values
 512 of profiles per altitude level. Temperature varies up to 10 K at around 11 km, water vapour
 513 mass varies up to 38% at the Earth surface and O₃ mass varies up to 40% at around 16 km. The
 514 averaged continental surface albedo and skin temperature of France are 0.132 and 292 K,
 515 respectively. For the Mediterranean Sea, they are 0.07 and 296 K, respectively.



516 Figure 11. a) Vertical profiles of pressure (mb), temperature (K), and H₂O, O₃ and CO₂ number
 517 densities (atm-cm/km) for three summer atmospheres: France, Mediterranean Sea and
 518 MIDLATSUM atmosphere. b) Maximum difference of vertical profiles.

519

520 DART and MODTRAN-5 were run in full radiance mode (simulation with solar radiation and
 521 thermal emission), with the same sun viewing angle ($\theta_{\text{sun}} = 30^\circ$, $\varphi_{\text{sun}} = 225^\circ$), surface
 522 parameters, discrete altitude levels, pressure, temperature profiles and gas number density
 523 profiles. Eq. (15) indicates how the gas optical depth was adjusted in DART using the user-
 524 defined density profiles $N_{m_i}(z)$ and $\rho_m^s(z)$.

$$\tau_{m_i}^a(\lambda) = \begin{cases} -\ln\left(t_{m_i,DB}^a(\lambda)\right) \cdot \frac{\int_0^\infty \sigma_{m_i,DB}^a(\lambda, z) \cdot N_{m_i}(z) dz}{\int_0^\infty \sigma_{m_i,DB}^a(\lambda, z) \cdot N_{m_i,DB}(z) dz}, & m_i = \text{H}_2\text{O}, \text{CO}_2, \text{O}_3, \text{CH}_4, \text{N}_2\text{O} \\ -\ln\left(t_{m_i,DB}^a(\lambda)\right) \cdot \frac{\int_0^\infty \sigma_{m_i}^a(\lambda) \cdot N_{m_i}(z) dz}{\int_0^\infty \sigma_{m_i}^a(\lambda) \cdot N_{m_i,DB}(z) dz}, & m_i \neq \text{H}_2\text{O}, \text{CO}_2, \text{O}_3, \text{CH}_4, \text{N}_2\text{O} \end{cases} \quad (15)$$

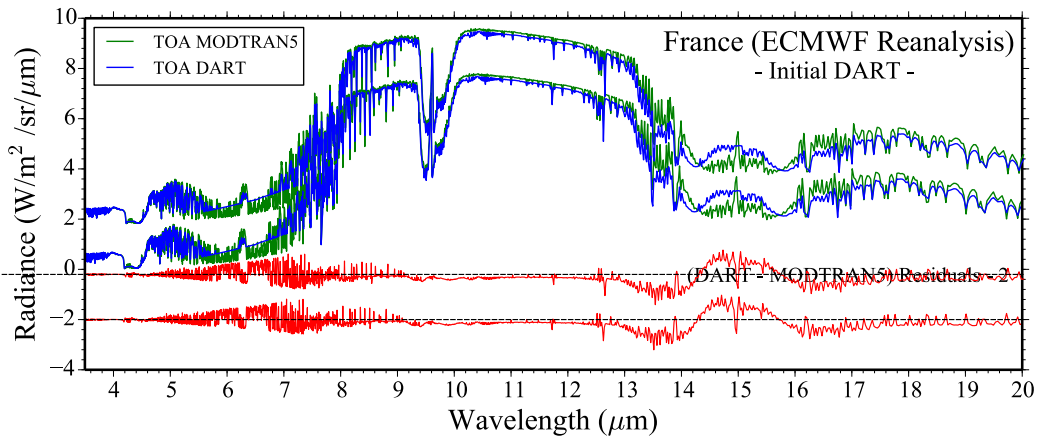
$$\tau^s(\lambda) = -\ln\left(t_{m,DB}^s(\lambda)\right) \cdot \frac{\int_0^\infty \rho_m^s(z) dz}{\int_0^\infty \rho_{m,DB}^s(z) dz}$$

525

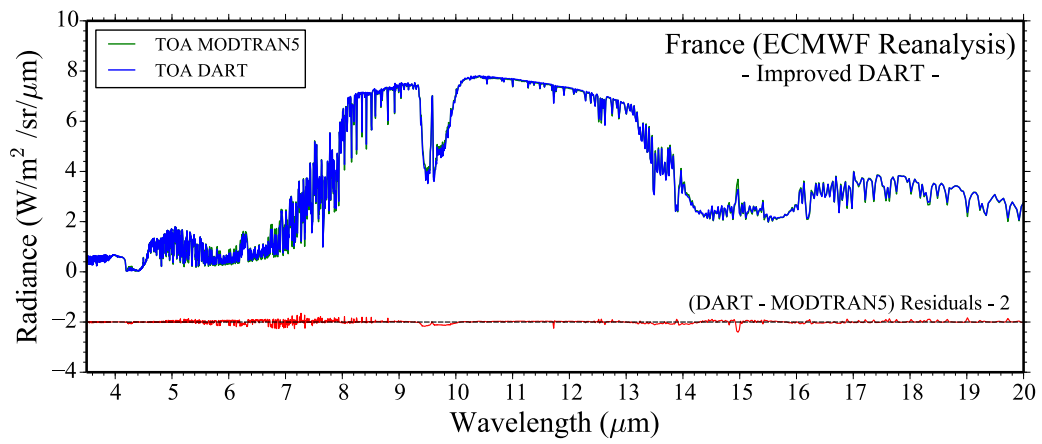
526 Note that m_i represents 13 gases (H₂O, O₃, N₂, CO₂, CO, CH₄, N₂O, O₂, NH₃, NO, NO₂, SO₂,
 527 HNO₃) and the sum of other minor gases (CFC₁₂, CFC₁₃, CFC₁₄, CFC₂₂, CFC₁₁₃, CFC₁₁₄,
 528 CFC₁₁₅, CLONO₂, HNO₄, CHCL₂F, CCL₄, N₂O₅).

529

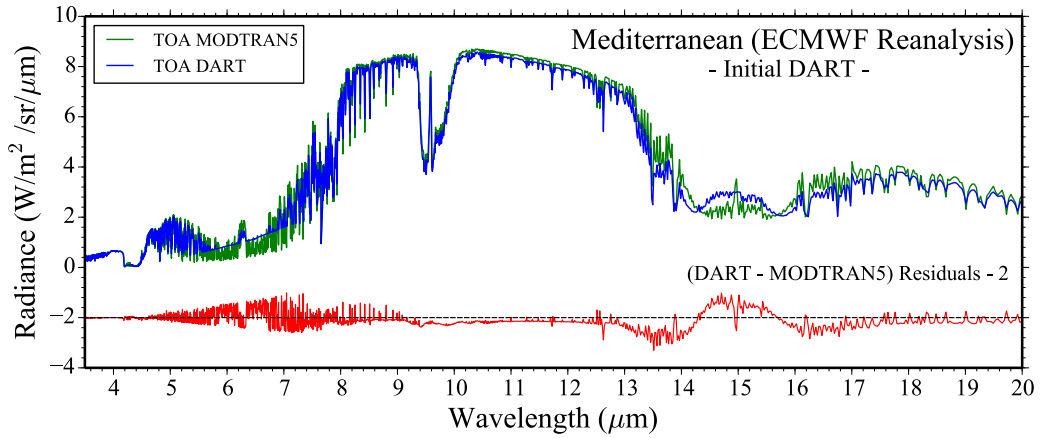
530 Figure 12 shows the MODTRAN-5 and initial and improved DART TOA nadir radiance spectra
 531 over France and Mediterranean Sea. BT MAE is reduced from 3.6 K to 1.0 K for France summer
 532 atmosphere, and from 3.7 K to 1.0 K for the Mediterranean Sea summer atmosphere. We can
 533 note that the residuals between improved DART and MODTRAN-5 over [3.5 μm , 5.0 μm]
 534 region where solar radiation contributes most to TOA radiance is relatively small (< 0.1
 535 $\text{W}/\text{m}^2/\text{sr}/\mu\text{m}$ for both cases). Also, the BT MAE in this region is less than 1.0 K. It confirms the
 536 accuracy of DART in this spectral region.



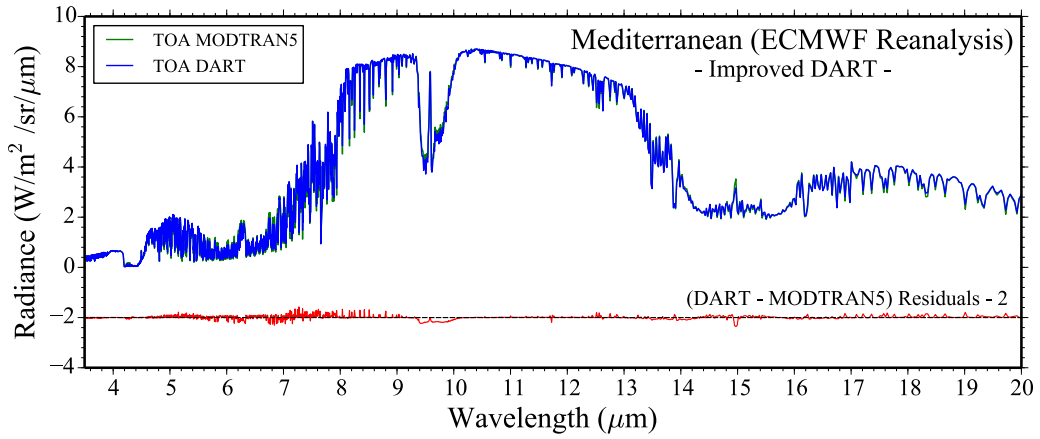
a)



b)



c)



d)

538 Figure 12. TOA spectral radiance of initial (a, c) and improved (b, d) DART compared to MODTRAN-
 539 5 with ECMWF reanalysis profile and surface parameter. a, b) France. c, d) Mediterranean
 540 Sea.

541

542 5.3 Discussion

543

544 As indicated in section 4, gas equivalent absorption cross-sections $\sigma_{m_i}^a(\lambda, z)$ per atmosphere
 545 altitude z and gas m_i are computed with Beer's law. However, Beer's law is less correct in the
 546 spectral bands with strong varying spectral absorption. In this case, the absorption extinction
 547 coefficient $\alpha_{j,m_i}^a(\lambda)$ computed by Eq. (9) is slightly smaller than the exact absorption extinction
 548 coefficient computed line-by-line, with a difference that depends on the number, strength and
 549 width of the absorption lines in the spectral bin. The small BT MAE with MODTRAN-5
 550 validates our strategy. Indeed, if Beer's law is not obeyed, the slightly smaller absorption
 551 extinction coefficients lead to slightly lower radiation attenuation and thermal emission that
 552 tend to compensate each other, which explains that DART results are accurate. For oblique
 553 directions, the longer line-of-sight in each layer increases the issue. Therefore, errors increase
 554 with the obliquity of viewing direction at TOA. Conversely, at the BOA, errors decrease with
 555 the obliquity of the viewing direction. Indeed, at BOA, the underestimated attenuation

556 compensates the underestimated thermal emission because the downward vector sources
557 depend more on the thermal emission of the lower atmosphere layers if the line-of-sight is more
558 oblique.

559

560 The equivalent absorption cross-sections were pre-computed for six standard atmospheres that
561 are representative of most pressure and temperature profiles in different seasons over our planet.

562 It explains that DART can simulate accurate TOA radiance spectra for most user-defined
563 atmospheres using the modelling method presented in section 5.2. However, results are less

564 accurate if the actual atmosphere greatly differs from the six standard atmospheres since the
565 pre-computed equivalent absorption cross-sections are for temperature and pressure profiles of

566 standard atmospheres. Although pressure profiles are relatively stable over the Earth,
567 temperature profiles vary with time and space. For this reason, we investigated the variation of

568 DART atmosphere thermal radiance accuracy if the atmosphere vertical profile is offset by ΔT
569 at all altitude levels. Figure 13.a illustrates the impact of an offset equal to +15 K for the

570 USSTD76 atmosphere, in thermal emission mode, no aerosol, with Earth skin temperature 0 K
571 and albedo 0.0. As expected, the offset increases the TOA BT MAE to 1.69 K, especially in the

572 $[10 \mu\text{m}, 13 \mu\text{m}]$ region where the DART adjustment method (Eq. (15)) overestimates vertical
573 optical depth, which leads to overestimated atmospheric TIR radiance. Table 9 shows the MAE

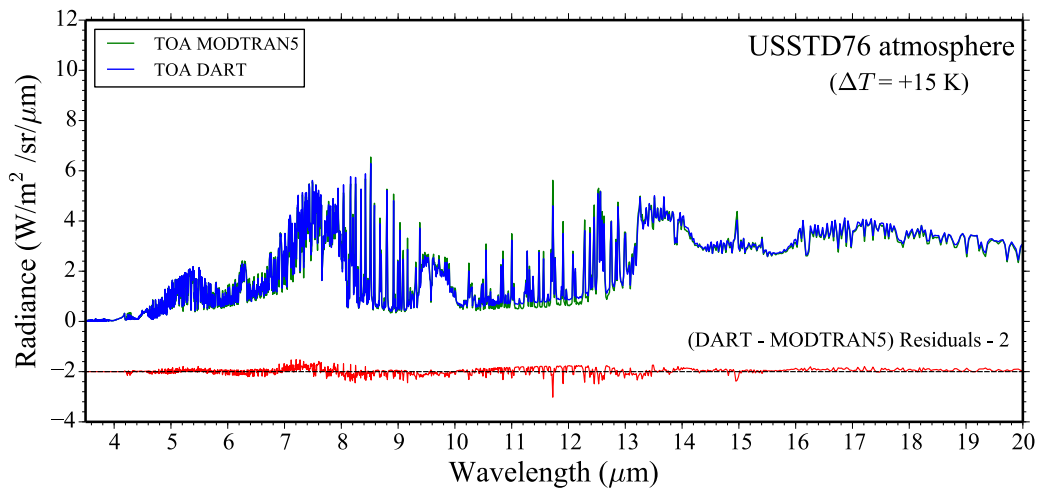
574 of TOA atmospheric TIR radiance of the USSTD76 atmosphere with five temperature offsets
575 $\Delta T = 3 \text{ K}, 6 \text{ K}, 9 \text{ K}, 12 \text{ K}$ and 15 K . Results are still accurate if the temperature offset relative

576 to the standard atmosphere is not too large. For example, TOA BT MAE is 1.07 K if $\Delta T = 6 \text{ K}$
577 and 1.27 K if $\Delta T = 9 \text{ K}$.

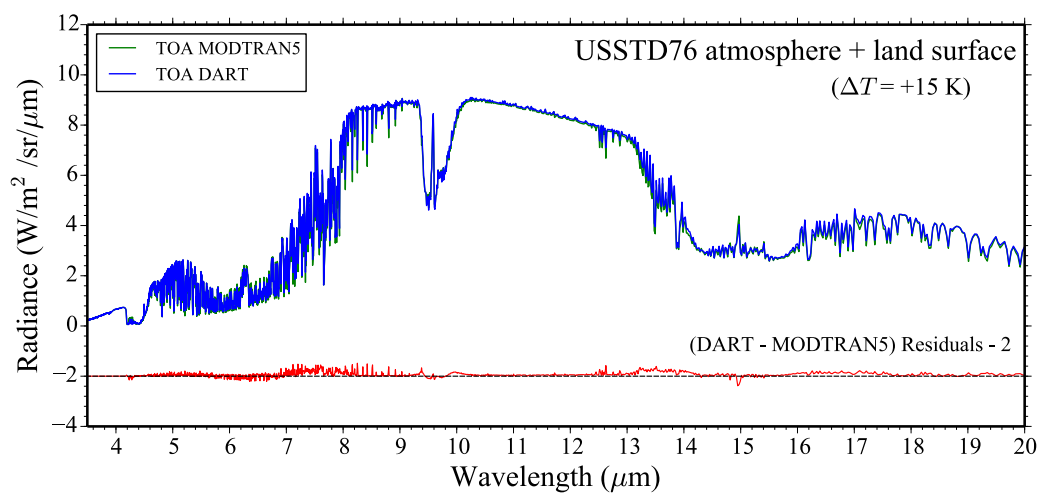
578

579 We must note the errors in Table 9 decrease if the Earth surface thermal emission and scattering
580 are considered. For example, Figure 13.b shows the DART and MODTRAN-5 TOA total

581 radiance spectra of the USSTD76 atmosphere with +15 K temperature offset, and a land surface
 582 with a skin temperature of 303.1 K (BOA temperature of the USSTD76 atmosphere with +15
 583 K offset) and an albedo of 0.14 (global annual average albedo of the Earth's surface in 2019
 584 derived from ERA-Interim dataset). Results are much better, with TOA BT MAE equal to 1.1
 585 K. Indeed, in the $[10 \mu\text{m}, 13 \mu\text{m}]$ region, the overestimated vertical optical depth slightly
 586 reduces the contribution of Earth surface thermal emission on TOA radiance. Then, the
 587 underestimated Earth thermal emission compensates the overestimated atmospheric thermal
 588 emission and the total TOA radiance is better.
 589



a)



b)

590 Figure 13. DART and MODTRAN-5 TOA TIR radiance spectra of the USSTD76 atmosphere with
 591 temperature vertical profile offset by +15 K. Atmosphere thermal emission only (a), total
 592 TOA thermal radiance with Earth surface thermal emission and scattering (b).

593 Table 9. TOA BT MAE of the USSTD76 atmosphere with six offsets ΔT of its temperature vertical
 594 profile.

ΔT	0 K	+3 K	+6 K	+9 K	+12 K	+15 K
BT MAE (K)	0.68	0.87	1.07	1.27	1.48	1.69

595

596 6. Concluding remarks

597

598 DART TIR atmospheric RT modelling accuracy has been greatly improved by (1) introducing
 599 the equivalent absorption cross-section of the five most absorbing gases (H₂O, CO₂, O₃, CH₄,
 600 N₂O) in six standard atmospheres (USSTD76, TROPICAL, MIDLATSUM, MIDLATWIN,
 601 SUBARCSUM, SUBARCWIN), and (2) implementing a double-layer thermal emission
 602 modelling method. MODTRAN-5, with its atmospheric thermal BT accuracy better than 1 K,
 603 is the reference atmospheric RT model to validate this improvement.

604

605 With the new RT modelling strategy, the TIR BT average MAE over the whole [3.5 μ m, 20
 606 μ m] region, for six standard atmospheres, decreased from 3.1 K to 0.71 K at TOA and from 2.1
 607 K to 0.64 K at BOA, with largest improvements in the TIR absorbing regions (*i.e.*, 3.5-4.5 μ m,
 608 6-7 μ m, 9-10 μ m, 14-16 μ m). The band BT error in TIR bands of present and future EO satellite
 609 missions is also reduced below the NeDT of satellite TIR sensors.

610

611 Sensitivity studies showed that DART atmospheric thermal radiance accuracy remains good (<
612 1 K) for oblique viewing zenith angle less than 50°. This improvement was also verified with
613 atmospheric profiles and surface parameters from the ECMWF reanalysis dataset for two large
614 zones: France and Mediterranean Sea during summer. The average differences of TOA radiance
615 spectra with MODTRAN-5 decreased from 3.6 K to 1.0 K for the France summer atmosphere,
616 and from 3.7 K to 1.0 K for the Mediterranean Sea summer atmosphere. In the spectral region
617 over 3.5-5.0 μm where the solar radiation contributes most to TOA radiance, the improved
618 DART still have accuracy better than 1.0 K.

619

620 DART atmospheric thermal radiance is less accurate if the user-defined atmosphere
621 temperature profile differs from the six standard atmospheres, because DART uses
622 temperature-dependent equivalent absorption cross-sections that are pre-computed for those
623 standard atmospheres. However, the decrease in accuracy is relatively small. For example, TOA
624 BT MAE only increases from 0.68 K to 1.07 K if the temperature profile of the USSTD76
625 atmosphere is offset by +6 K. In addition, the MAE decreases if the Earth surface thermal
626 emission and scattering is considered. Future work will investigate a better adjustment method
627 to compute accurate gas optical depth for arbitrary atmosphere profiles.

628

629 Due to its accurate TIR RT modelling both in the atmosphere and in 3D urban and natural
630 landscapes, including the Earth-atmosphere radiative coupling, DART meets the requirements
631 of TIR EO satellite missions (*i.e.*, Trishna, Sentinel 3, Landsat 8/9) and LST applications in the
632 remote sensing community, which opens new perspectives for DART model.

633

634 **Acknowledgements**

635

636 This work is funded by Région Occitanie Pyrénées-Méditerranée, France and the TOSCA
 637 program of French Space Agency (CNES). We are also grateful for the support of DART team
 638 scientists (Dr N. Lauret, J. Guilleux, E. Chavanon), and also to Dr A. Berk (Spectral Sciences,
 639 USA) and Dr T. Yin (NASA, USA) for advices on MODTRAN-5 model.

640

641 **Appendix. Nomenclature**

642

Symbols	Definitions
ΔS	Surface
ΔL	Horizontal path length
H	Scale height for major gases of an average atmosphere
Ω	Direction vector
$\Delta\Omega$	Solid angle of direction Ω
θ	Zenith angle
μ	Shorthand of $\cos(\theta)$
φ	Azimuth angle
λ	Wavelength
$\Delta\lambda$	Bandwidth
j	Index of atmosphere layer
J	Number of DART atmosphere layers
k	Index of virtual sub-layer
k_j	Number of virtual sub-layers in layer j
z	Altitude
z_{j-1}	Lower boundary altitude of layer j

z_j	Upper boundary altitude of layer j
Δz_j	Thickness of layer j
Δz_k	Thickness of virtual sub-layer k
$Z_{m_i}^*$	Specific height defined per gas m_i such that under this altitude over 98% of gas m_i is concentrated.
h	Relative altitude within a layer j , with $h = 0$ at bottom of layer and $h = \Delta z_j$ at top of layer
$T(z)$	Temperature profile
ΔT	Temperature offset
$T_j(h)$	Temperature at relative altitude h in layer j
T_x, T_y	Temperature variables in the double-layer method
T_j^U	Upper boundary temperature of layer j
T_j^L	Lower boundary temperature of layer j
T_j	Average temperature of layer j
T_{k-1}	Lower boundary temperature of virtual sub-layer k
T_k	Upper boundary temperature of virtual sub-layer k
$T_{DB}(z)$	Temperature profile in DART atmosphere database
$P(z)$	Pressure profile
$P_{DB}(z)$	Pressure profile in DART atmosphere database
$N(z)$	Number density profile
$N_m^s(z)$	Number density profile of scattering gases
$N_{m_i}(z)$	Number density profile of gas m_i
$N_{m_i,DB}(z)$	Number density profile of gas m_i in DART atmosphere database
$\rho_{m,DB}^s(z)$	Relative density profile of scattering gases in DART atmosphere database

$t_{m_i}^a(\lambda)$	Vertical absorption transmittance of gas m_i at wavelength λ
$t_{m_i}^a(\lambda, z, \Delta L)$	Absorption transmittance of gas m_i at wavelength λ along horizontal path ΔL at altitude z
$t_{m_i,DB}^a(\lambda)$	Vertical absorption transmittance of gas m_i at wavelength λ in DART atmosphere database
$t_m^s(\lambda)$	Vertical scattering transmittance of scattering gases at wavelength λ
$t_{m,DB}^s(\lambda)$	Vertical scattering transmittance of scattering gases at wavelength λ in DART atmosphere database
$\tau_{m_i}^a(\lambda)$	Vertical absorption optical depth of gas m_i at wavelength λ
$\tau^s(\lambda)$	Vertical scattering optical depth of scattering gases at wavelength λ
$\tau_p(\lambda)$	Vertical optical depth of aerosols at wavelength λ
$\tau_{p,DB}(\lambda)$	Vertical optical depth of aerosols at wavelength λ in DART atmosphere database
$\Delta\tau_j(\lambda)$	Total optical depth of gases and aerosols of layer j at wavelength λ
$\tau_{j-1}(\lambda)$	Optical depth of gases and aerosols at bottom of layer j at wavelength λ
$\tau_j(\lambda)$	Optical depth of gases and aerosols at top of layer j at wavelength λ
$\tau_{k-1}(\lambda)$	Optical depth of gases and aerosols at bottom of virtual sub-layer k at wavelength λ
$\tau_k(\lambda)$	Optical depth of gases and aerosols at top of virtual sub-layer k at wavelength λ
$\Delta\tau_k(\lambda)$	Total optical depth of gases and aerosols of virtual sub-layer k at wavelength λ
$\tau_j(\lambda, h)$	Optical depth profile at wavelength λ at relative attitude h in layer j
$A_j(\lambda), B_j(\lambda)$	Coefficients of optical depth function in layer j at wavelength λ

$C_j(\lambda), D_j(\lambda)$

α^e	Total extinction coefficient
α^a	Absorption extinction coefficient
α^s	Scattering extinction coefficient
α_0^e	Total extinction coefficient at bottom of atmosphere
$\alpha_{j,m_i}^a(\lambda)$	Absorption extinction coefficient of gas m_i of layer j at wavelength λ
$\alpha_{j,m}^a(\lambda)$	Gas absorption extinction coefficient of layer j at wavelength λ
$\alpha_{j,m}^s(\lambda)$	Gas scattering extinction coefficient of layer j at wavelength λ
$\alpha_{j,m}^e(\lambda)$	Gas total extinction coefficient of layer j at wavelength λ
$\alpha_{j,p}^a(\lambda)$	Aerosol absorption extinction coefficient of layer j at wavelength λ
$\alpha_{j,p}^s(\lambda)$	Aerosol scattering extinction coefficient of layer j at wavelength λ
$\alpha_{j,p}^e(\lambda)$	Aerosol total extinction coefficient of layer j at wavelength λ
$\alpha_{p,DB}^e(z)$	Aerosol total extinction coefficient profile at 550 nm in DART atmosphere database
$\alpha_j^a(\lambda)$	Total absorption extinction coefficient of gases and aerosols of layer j at wavelength λ
$\alpha_j^s(\lambda)$	Total scattering extinction coefficient of gases and aerosols of layer j at wavelength λ
$\alpha_j^e(\lambda)$	Total extinction coefficient of gases and aerosols of layer j at wavelength λ
$\alpha_j^e(\lambda, h)$	Extinction coefficient profile of gases and aerosols at wavelength λ at relative altitude h in layer j
$\alpha_{z_{j-1}}^e(\lambda)$	Total extinction coefficient of gases and aerosols at lower boundary of layer j at wavelength λ

$\alpha_{z_j}^e(\lambda)$	Total extinction coefficient of gases and aerosols at upper boundary of layer j at wavelength λ
$\sigma_{m_i}^a(\lambda)$	Absorption cross-section of gas m_i at wavelength λ
$\sigma_m^s(\lambda)$	Gas scattering cross-section at wavelength λ
$\sigma_{m_i}^a(\lambda, z, \Delta L)$	Equivalent absorption cross-section of gas m_i at wavelength λ along horizontal path ΔL at altitude z
$\sigma_{m_i}^{a(*)}(\lambda, z, \Delta L)$	Rescaled $\sigma_{m_i}^a(\lambda, z, \Delta L)$ by dividing $\sigma_{m_i}^a(\lambda, z = 0, \Delta L)$
$\sigma_{m_i}^a(\lambda, z)$	Equivalent absorption cross-section of gas m_i at wavelength λ along horizontal path $\Delta L = 7$ km at altitude z
$\omega_{p,DB}(\lambda)$	Aerosol single scattering albedo at wavelength λ in DART atmosphere database
$\omega_j(\lambda)$	Single scattering albedo of mixed gases and aerosols of layer j at wavelength λ
$W_j(\Omega, \lambda)$	Vector source of layer j along direction Ω at wavelength λ
$W_j^\uparrow(\Omega, \lambda)$	Upward vector source of layer j along direction Ω at wavelength λ
$W_j^\downarrow(\Omega, \lambda)$	Downward vector source of layer j along direction Ω at wavelength λ
$L_B(T, \lambda)$	Planck function at temperature T at wavelength λ
$W_{\text{ref}}^\uparrow(\Omega, \lambda)$	Spectrum of reference upward vector source along direction Ω at wavelength λ
ε	Threshold corresponds to MODTRAN decimal precision
q	Band index
Q	Number of spectral bands
$X_{\text{DART}}(q)$	A type of DART product at band q
$X_{\text{MODTRAN}}(q)$	A type of MODTRAN product at band q

MAE	Mean absolute error
MARE	Mean absolute relative error

643

644 **References**

645

646 Abramowitz, M., Stegun, I.A., 1948. Handbook of mathematical functions with formulas,
647 graphs, and mathematical tables. US Government printing office.

648 Anderson, G.P., Clough, S.A., Kneizys, F.X., Chetwynd, J.H., Shettle, E.P., 1986. AFGL
649 atmospheric constituent profiles (0.120 km). AIR FORCE GEOPHYSICS LAB
650 HANSCOM AFB MA.

651 Bento, V.A., DaCamara, C.C., Trigo, I.F., Martins, J., Duguay-Tetzlaff, A., 2017. Improving
652 land surface temperature retrievals over mountainous regions. Remote Sens. 9, 38.

653 Berk, A., Anderson, G.P., Acharya, P.K., Bernstein, L.S., Muratov, L., Lee, J., Fox, M., Adler-
654 Golden, S.M., Chetwynd, J.H., Hoke, M.L., 2005. MODTRAN 5: a reformulated
655 atmospheric band model with auxiliary species and practical multiple scattering options:
656 update, in: Algorithms and Technologies for Multispectral, Hyperspectral, and
657 Ultraspectral Imagery XI. International Society for Optics and Photonics, pp. 662–667.

658 Berk, A., Anderson, G.P., Acharya, P.K., Shettle, E.P., 2008. MODTRAN5. 2.0. 0 user's
659 manual. Spectr. Sci. Inc., Burlingt. MA, Air Force Res. Lab. Hanscom MA.

660 Berk, A., Bernstein, L.S., Robertson, D.C., 1987. MODTRAN: A moderate resolution model
661 for LOWTRAN. SPECTRAL SCIENCES INC BURLINGTON MA.

662 Berk, A., Conforti, P., Hawes, F., 2015. An accelerated line-by-line option for MODTRAN
663 combining on-the-fly generation of line center absorption within 0.1 cm⁻¹ bins and pre-
664 computed line tails, in: Algorithms and Technologies for Multispectral, Hyperspectral, and
665 Ultraspectral Imagery XXI. International Society for Optics and Photonics, p. 947217.

666 Bodhaine, B.A., Wood, N.B., Dutton, E.G., Slusser, J.R., 1999. On Rayleigh optical depth
667 calculations. *J. Atmos. Ocean. Technol.* 16, 1854–1861.

668 Bonafoni, S., 2016. Downscaling of Landsat and MODIS land surface temperature over the
669 heterogeneous urban area of Milan. *IEEE J. Sel. Top. Appl. Earth Obs. Remote Sens.* 9,
670 2019–2027.

671 Buehler, S.A., Mendrok, J., Eriksson, P., Perrin, A., Larsson, R., Lemke, O., 2018. ARTS, the
672 Atmospheric Radiative Transfer Simulator-version 2.2. *Geosci. Model Dev.* 11, 1537–
673 1556.

674 Clough, S.A., Iacono, M.J., Moncet, J., 1992. Line-by-line calculations of atmospheric fluxes
675 and cooling rates: Application to water vapor. *J. Geophys. Res. Atmos.* 97, 15761–15785.

676 Clough, S.A., Shephard, M.W., Mlawer, E.J., Delamere, J.S., Iacono, M.J., Cady-Pereira, K.,
677 Boukabara, S., Brown, P.D., 2005. Atmospheric radiative transfer modeling: a summary
678 of the AER codes. *J. Quant. Spectrosc. Radiat. Transf.* 91, 233–244.

679 Donlon, C., Berruti, B., Buongiorno, A., Ferreira, M.-H., Féménias, P., Frerick, J., Goryl, P.,
680 Klein, U., Laur, H., Mavrocordatos, C., 2012. The global monitoring for environment and
681 security (GMES) sentinel-3 mission. *Remote Sens. Environ.* 120, 37–57.

682 Dugdale, S.J., 2016. A practitioner’s guide to thermal infrared remote sensing of rivers and
683 streams: recent advances, precautions and considerations. *Wiley Interdiscip. Rev. Water*
684 3, 251–268.

685 Ermida, S.L., Trigo, I.F., DaCamara, C.C., Roujean, J.-L., 2018. Assessing the potential of
686 parametric models to correct directional effects on local to global remotely sensed LST.
687 *Remote Sens. Environ.* 209, 410–422.

688 Gastellu-Etchegorry, J.-P., Demarez, V., Pinel, V., Zagolski, F., 1996. Modeling radiative
689 transfer in heterogeneous 3-D vegetation canopies. *Remote Sens. Environ.* 58, 131–156.

690 Gastellu-Etchegorry, J.-P., Lauret, N., Yin, T., Landier, L., Kallel, A., Malenovský, Z., Al Bitar,

691 A., Aval, J., Benhmida, S., Qi, J., 2017. DART: recent advances in remote sensing data
692 modeling with atmosphere, polarization, and chlorophyll fluorescence. *IEEE J. Sel. Top.*
693 *Appl. Earth Obs. Remote Sens.* 10, 2640–2649.

694 Gastellu-Etchegorry, J.-P., Yin, T., Lauret, N., Cajgfinger, T., Gregoire, T., Grau, E., Feret, J.-
695 B., Lopes, M., Guilleux, J., Dedieu, G., 2015. Discrete anisotropic radiative transfer
696 (DART 5) for modeling airborne and satellite spectroradiometer and LIDAR acquisitions
697 of natural and urban landscapes. *Remote Sens.* 7, 1667–1701.

698 Gastellu-Etchegorry, J.P., Martin, E., Gascon, F., 2004. DART: a 3D model for simulating
699 satellite images and studying surface radiation budget. *Int. J. Remote Sens.* 25, 73–96.

700 Grau, E., Gastellu-Etchegorry, J.-P., 2013. Radiative transfer modeling in the Earth–
701 Atmosphere system with DART model. *Remote Sens. Environ.* 139, 149–170.

702 Guillevic, P., Gastellu-Etchegorry, J.P., Demarty, J., Prévot, L., 2003. Thermal infrared
703 radiative transfer within three-dimensional vegetation covers. *J. Geophys. Res. Atmos.*
704 108.

705 Guillevic, P.C., Bork-Unkelbach, A., Göttsche, F.M., Hulley, G., Gastellu-Etchegorry, J.-P.,
706 Olesen, F.S., Privette, J.L., 2013. Directional viewing effects on satellite land surface
707 temperature products over sparse vegetation canopies—A multisensor analysis. *IEEE*
708 *Geosci. Remote Sens. Lett.* 10, 1464–1468.

709 He, J., Zhao, W., Li, A., Wen, F., Yu, D., 2019. The impact of the terrain effect on land surface
710 temperature variation based on Landsat-8 observations in mountainous areas. *Int. J.*
711 *Remote Sens.* 40, 1808–1827.

712 Huang, H., 2018. Accelerated RAPID model using heterogeneous porous objects. *Remote Sens.*
713 10, 1264.

714 Irons, J.R., Dwyer, J.L., Barsi, J.A., 2012. The next Landsat satellite: The Landsat data
715 continuity mission. *Remote Sens. Environ.* 122, 11–21.

716 Jacquinet-Husson, N., Armante, R., Scott, N.A., Chédin, A., Crépeau, L., Boutammine, C.,
717 Bouhdaoui, A., Crevoisier, C., Capelle, V., Boone, C., 2016. The 2015 edition of the
718 GEISA spectroscopic database. *J. Mol. Spectrosc.* 327, 31–72.

719 Khanal, S., Fulton, J., Shearer, S., 2017. An overview of current and potential applications of
720 thermal remote sensing in precision agriculture. *Comput. Electron. Agric.* 139, 22–32.

721 Kilpatrick, K.A., Podestá, G., Walsh, S., Williams, E., Halliwell, V., Szczodrak, M., Brown,
722 O.B., Minnett, P.J., Evans, R., 2015. A decade of sea surface temperature from MODIS.
723 *Remote Sens. Environ.* 165, 27–41.

724 Kobayashi, H., Iwabuchi, H., 2008. A coupled 1-D atmosphere and 3-D canopy radiative
725 transfer model for canopy reflectance, light environment, and photosynthesis simulation
726 in a heterogeneous landscape. *Remote Sens. Environ.* 112, 173–185.

727 Lagouarde, J.-P., Bhattacharya, B.K., Crebassol, P., Gamet, P., Babu, S.S., Boulet, G., Briottet,
728 X., Buddhiraju, K.M., Cherchali, S., Dadou, I., 2018. The Indian-French Trishna mission:
729 Earth observation in the thermal infrared with high spatio-temporal resolution, in:
730 IGARSS 2018-2018 IEEE International Geoscience and Remote Sensing Symposium.
731 IEEE, pp. 4078–4081.

732 Li, Z.-L., Tang, B.-H., Wu, H., Ren, H., Yan, G., Wan, Z., Trigo, I.F., Sobrino, J.A., 2013.
733 Satellite-derived land surface temperature: Current status and perspectives. *Remote Sens.*
734 *Environ.* 131, 14–37.

735 McCorkel, J., Montanaro, M., Efremova, B., Pearlman, A., Wenny, B., Lunsford, A., Simon,
736 A., Hair, J., Reuter, D., 2018. Landsat 9 Thermal Infrared Sensor 2 Characterization Plan
737 Overview, in: IGARSS 2018-2018 IEEE International Geoscience and Remote Sensing
738 Symposium. IEEE, pp. 8845–8848.

739 Press, W.H., Teukolsky, S.A., Vetterling, W.T., Flannery, B.P., 2007. Numerical recipes 3rd
740 edition: The art of scientific computing. Cambridge university press.

741 Price, J.C., 1983. Estimating surface temperatures from satellite thermal infrared data—A
742 simple formulation for the atmospheric effect. *Remote Sens. Environ.* 13, 353–361.

743 Rothman, L.S., Gordon, I.E., Barbe, A., Benner, D.C., Bernath, P.F., Birk, M., Boudon, V.,
744 Brown, L.R., Campargue, A., Champion, J.-P., 2009. The HITRAN 2008 molecular
745 spectroscopic database. *J. Quant. Spectrosc. Radiat. Transf.* 110, 533–572.

746 Scott, N.A., 1974. A direct method of computation of the transmission function of an
747 inhomogeneous gaseous medium—I: Description of the method. *J. Quant. Spectrosc.*
748 *Radiat. Transf.* 14, 691–704.

749 Shettle, E.P., Fenn, R.W., 1979. Models for the aerosols of the lower atmosphere and the effects
750 of humidity variations on their optical properties. Optical Physics Division, Air Force
751 Geophysics Laboratory.

752 Sobrino, J.A., Del Frate, F., Drusch, M., Jiménez-Muñoz, J.C., Manunta, P., Regan, A., 2016.
753 Review of thermal infrared applications and requirements for future high-resolution
754 sensors. *IEEE Trans. Geosci. Remote Sens.* 54, 2963–2972.

755 Verhoef, W., 1984. Light scattering by leaf layers with application to canopy reflectance
756 modeling: The SAIL model. *Remote Sens. Environ.* 16, 125–141.

757 Vermote, E.F., El Saleous, N.Z., Justice, C.O., 2002. Atmospheric correction of MODIS data
758 in the visible to middle infrared: first results. *Remote Sens. Environ.* 83, 97–111.

759 Vincent, R.A., Dudhia, A., 2017. Fast radiative transfer using monochromatic look-up tables.
760 *J. Quant. Spectrosc. Radiat. Transf.* 186, 254–264.

761 Voogt, J.A., Oke, T.R., 2003. Thermal remote sensing of urban climates. *Remote Sens. Environ.*
762 86, 370–384.

763 Wang, K., Li, Z., Cribb, M., 2006. Estimation of evaporative fraction from a combination of
764 day and night land surface temperatures and NDVI: A new method to determine the
765 Priestley–Taylor parameter. *Remote Sens. Environ.* 102, 293–305.

- 766 Wang, L., Qu, J.J., 2009. Satellite remote sensing applications for surface soil moisture
767 monitoring: A review. *Front. Earth Sci. China* 3, 237–247.
- 768 Widlowski, J.-L., Lavergne, T., Pinty, B., Verstraete, M., Gobron, N., 2006. Rayspread: A
769 virtual laboratory for rapid BRDF simulations over 3-D plant canopies, in: *Computational*
770 *Methods in Transport*. Springer, pp. 211–231.
- 771 Widlowski, J.-L., Mio, C., Disney, M., Adams, J., Andredakis, I., Atzberger, C., Brennan, J.,
772 Busetto, L., Chelle, M., Ceccherini, G., 2015. The fourth phase of the radiative transfer
773 model intercomparison (RAMI) exercise: Actual canopy scenarios and conformity testing.
774 *Remote Sens. Environ.* 169, 418–437.
- 775 Widlowski, J., Pinty, B., Lopatka, M., Atzberger, C., Buzica, D., Chelle, M., Disney, M.,
776 Gastellu-Etchegorry, J., Gerboles, M., Gobron, N., 2013. The fourth radiation transfer
777 model intercomparison (RAMI-IV): Proficiency testing of canopy reflectance models with
778 ISO-13528. *J. Geophys. Res. Atmos.* 118, 6869–6890.
- 779 Widlowski, J., Taberner, M., Pinty, B., Bruniquel-Pinel, V., Disney, M., Fernandes, R.,
780 Gastellu-Etchegorry, J., Gobron, N., Kuusk, A., Lavergne, T., 2007. Third Radiation
781 Transfer Model Intercomparison (RAMI) exercise: Documenting progress in canopy
782 reflectance models. *J. Geophys. Res. Atmos.* 112.
- 783 Willmott, C.J., Matsuura, K., 2005. Advantages of the mean absolute error (MAE) over the root
784 mean square error (RMSE) in assessing average model performance. *Clim. Res.* 30, 79–
785 82.
- 786 Wiscombe, W.J., 1976. Extension of the doubling method to inhomogeneous sources. *J. Quant.*
787 *Spectrosc. Radiat. Transf.* 16, 477–489.

788

789 **List of Figure Captions**

790

791 Figure 1. DART 3D mock-up and voxel matrix. Atmosphere is separated in three altitude
792 regions: high atmosphere (HA) made of layers, mid-atmosphere (MA) made of voxels of any
793 size, and bottom atmosphere (BA) in the Earth scene. Earth scene elements are made of facets
794 (triangles), and/or fluid and turbid vegetation voxels. The voxel matrix is introduced to optimize
795 ray tracing.

796

797 Figure 2. DART horizontally homogeneous atmosphere layer with layer thickness Δz_j . The
798 upper and lower boundary parameters are marked.

799

800 Figure 3. Major steps for modelling the RT in the Earth-atmosphere system. Red colour
801 indicates thermal emission (steps 1 and 2), orange colour indicates solar incident radiation, and
802 yellow colour indicates thermal and/or solar radiation that is scattered.

803

804 Figure 4. Initial DART and MODTRAN-5 TOA / BOA TIR radiance in $[3.5 \mu\text{m}, 20 \mu\text{m}]$ region
805 for USSTD76 (a), TROPICAL (b), MIDLATSUM (c) and SUBARCWIN (d) atmospheres. 1
806 cm^{-1} spectral resolution. DART and MODTRAN-5 configurations are detailed in section 3.

807

808 Figure 5. CO_2 equivalent absorption cross-section $\sigma_{m_i}^a(\lambda, z, \Delta L)$ (a, c) and rescaled equivalent
809 absorption cross-section $\sigma_{m_i}^{a(*)}(\lambda, z, \Delta L)$ (b, d) at $13.4 \mu\text{m}$ (a, b) and $13.1 \mu\text{m}$ (c, d), in a 1 cm^{-1}
810 spectral bin, for 4 identical horizontal paths ($\Delta L = 1 \text{ km}, 2 \text{ km}, 5 \text{ km}, 10 \text{ km}$) at altitudes up to
811 25 km for $13.4 \mu\text{m}$ and up to 15 km for $13.1 \mu\text{m}$, in the USSTD76 atmosphere.

812

813 Figure 6. Profiles of DART initial and improved absorption extinction coefficients in the
814 USSTD76 atmosphere. a) $10.0 \mu\text{m}$. b) $13.0 \mu\text{m}$. c) $15.4 \mu\text{m}$. d) $19.6 \mu\text{m}$. Spectral bin is 1 cm^{-1} .

815

816 Figure 7. DART atmosphere is made of J layers, with layer optical depth $\Delta\tau_j$ and layer
817 thickness Δz_j . Each layer j is virtually divided into k_j sub-layers, with sub-layer thickness
818 $\Delta z_k = \frac{\Delta z_j}{k_j}$ and sub-layer optical depth $\Delta\tau_k$, with upper and lower boundary temperature T_k and
819 T_{k-1} , respectively.

820

821 Figure 8. Difference of DART double-layer upward vector source compared with the reference,
822 for various numbers of sub-layers. T^U and T^L are respectively the upper and lower boundary
823 temperatures. TRANS represents the layer transmittance. MARE is marked in the legend.

824

825 Figure 9. Improved DART and MODTRAN-5 TOA / BOA TIR radiance in $[3.5 \mu\text{m}, 20 \mu\text{m}]$
826 region for USSTD76 (a), TROPICAL (b), MIDLATSUM (c) and SUBARCWIN (d)
827 atmospheres. 1 cm^{-1} spectral resolution. DART and MODTRAN-5 configurations are detailed
828 in section 3.

829

830 Figure 10. Improved DART and MODTRAN-5 TOA / BOA TIR radiance in $[3.5 \mu\text{m}, 20 \mu\text{m}]$
831 region for the USSTD76 atmosphere. Viewing zenith angle $\theta = 30^\circ$ (a) and $\theta = 60^\circ$ (b).

832

833 Figure 11. a) Vertical profiles of pressure (mb), temperature (K), and H_2O , O_3 and CO_2 number
834 densities (atm-cm/km) for three summer atmospheres: France, Mediterranean Sea and
835 MIDLATSUM atmosphere. b) Maximum difference of vertical profiles.

836

837 Figure 12. TOA spectral radiance of initial (a, c) and improved (b, d) DART compared to
838 MODTRAN-5 with ECMWF reanalysis profile and surface parameter. a, b) France. c, d)
839 Mediterranean Sea.

840

841 Figure 13. DART and MODTRAN-5 TOA TIR radiance spectra of the USSTD76 atmosphere
842 with temperature vertical profile offset by +15 K. Atmosphere thermal emission only (a), total
843 TOA thermal radiance with Earth surface thermal emission and scattering (b).